Gliogenesis from the subventricular zone modulates the extracellular matrix at the glial scar after brain ischemia

Maria Ardaya[1,2,3,9], Marie-Catherine Tiveron[4], Harold Cremer[4], Benjamin Dehay[5], Fernando Pérez-Cerdá[1,2,3], Carlos Matute[1,2,3], Federico N. Soria[1,2,3,6,*], Fabio Cavaliere[1,2,3,7,8,*]

[1]Achucarro Basque Center for Neuroscience, Leioa, Spain.

[2]Department of Neuroscience, University of the Basque Country (UPV/EHU), Leioa, Spain.

[3]CIBERNED, Madrid, Spain.

[4]Aix Marseille Univ, CNRS, IBDM, Campus de Luminy, Marseille, France.

[5]Univ. Bordeaux, CNRS, IMN, UMR 5293, F-33000 Bordeaux, France.

[6]Ikerbasque, Basque Foundation for Science, Bilbao, Spain.

[7]Basque Biomodel Platform for Human Research (BBioH), Leioa, Spain.

[8]Current Address: Instituto Biofisika (CSIC, UPV/EHU), Fundación Biofísica Bizkaia, Leioa, Spain

[9]Current Address: Donostia International Physics Center (DIPC), San Sebastian, Spain.

[*]Correspondence to fabio.cavaliere@ehu.eus (F.C.), federico.soria@achucarro.org (F.N.S.)

ABSTRACT

Activation of the subventricular zone (SVZ) following cerebral ischemia is one of the brain's early responses to counteract neuron loss and minimize tissue damage. Impaired brain regions communicate with the SVZ through various chemotactic signals that promote cell migration and differentiation, primarily involving neural stem cells (NSC), neuroblasts, or glioblasts. However, the activation of gliogenesis and the role of newly formed astrocytes in the post-ischemic scenario remain subjects of debate. We have previously demonstrated that adenosine release after brain ischemia prompts the SVZ to generate new astrocytes. Here, we used transient brain ischemia in mice to identify the cellular origin of these astrocytes within the SVZ neurogenic niche and to investigate their role in the pathological process. By combining immunofluorescence, BrdU-tracing, and genetic cell labeling, we tracked the migration of newborn astrocytes, positive for the proteoglycan marker Thbs4, from the dorsal and medial SVZ to the perilesional barrier surrounding the ischemic core, known as the "glial scar". We found that these Thbs4-positive astrocytes modulate the dense extracellular matrix at the lesion border by both synthesizing and degrading hyaluronan. We also show that while the accumulation of hyaluronan at the lesion site is sufficient to recruit newborn astrocytes, its degradation at the SVZ correlates with gliogenesis. These findings suggest that newborn astrocytes could be a promising pharmacological target for modulating the glial scar after brain ischemia and facilitate tissue regeneration.

37 **INTRODUCTION**

38 Cell regeneration in the adult mammalian brain primarily occurs in two neurogenic niches: the
39 subventricular zone (SVZ) in the lateral ventricle and the subgranular zone (SGZ) in the dentate gyrus
40 of the hippocampus (Bond et al., 2015). Adult brain stem cells are multipotent and originate from the
41 embryonic radial glia, thus sharing key cell markers and features with resident astrocytes. In the adult
42 mouse brain, neuroblasts from SVZ migrate through the rostral migratory stream (RMS) to the olfactory
43 bulb (OB), where neurogenesis takes place (Luskin, 1993). Neuronal hyperactivity (e.g., during
44 epilepsy), as well as pathological conditions (e.g., stroke) or natural (e.g., aging) processes, can impair
45 the physiological functions of the neurogenic niches, altering their neurogenic and gliogenic potential
46 (Chaker et al., 2016; Kralic et al., 2005; Sundholm-Peters et al., 2005). For instance, it is known that
47 SVZ cells are activated *in vivo* after focal ischemia following a middle cerebral artery occlusion
48 (MCAO) (Ceanga et al., 2021).

49 We have previously demonstrated in oxygen and glucose-deprived (OGD) organotypic brain slices that
50 the ischemic region and the SVZ establish a biochemical interplay based on a gradient of toxic and
51 protective factors released early after the insult (Cavaliere et al., 2006). Furthermore, others have
52 demonstrated that brain stroke models in mice can activate astrogliogenesis at the expense of
53 neurogenesis (Benner et al., 2013; Laug et al., 2019; Li et al., 2010). Benner and colleagues identified
54 a SVZ-derived astrocyte population characterized by high levels of the membrane-bound proteoglycan
55 thrombospondin 4 (Thbs4), a cell-cell and cell-matrix adhesion molecule that has been considered
56 neuroprotective against ischemic damage (Benner et al., 2013; Laug et al., 2019). Ablation of Thbs4 in
57 KO mice also produced abnormal ischemic scar formation and increased microvascular hemorrhage,
58 suggesting a role of SVZ astrogliogenesis in brain damage and glial scar formation induced by ischemic
59 stroke (Benner et al., 2013).

60 The perilesional barrier known as the *glial scar* assembles early after brain ischemia, isolating the
61 damaged area and limiting both the spread of pathogens and potentially toxic damage-associated
62 molecular patterns (DAMPs) into the surrounding area (Anderson et al., 2016; Bush et al., 1999;

63 Faulkner et al., 2004). Consisting of packed reactive astrocytes and a dense extracellular matrix
64 composed mostly of hyaluronic acid (HA), the glial scar represents a physical barrier for the SVZ-
65 generated newborn neurons that migrate into the ischemic core (Arvidsson et al., 2002; Yamashita et
66 al., 2006). Thus, modulating glial scar formation after brain ischemia may be a strategy to reduce tissue
67 damage and restore brain functionality. In ischemic stroke, the brain extracellular matrix (ECM) goes
68 through a significant reorganization due to injury and must undergo successful remodeling to promote
69 brain repair. ECM elements involved in the ischemic cascade induce activation of astrocytes and
70 microglia, which modulate ECM structure by releasing glycoproteins into the extracellular space
71 (Adams and Gallo, 2018; Fawcett, 2015). This crosstalk culminates in the formation of the glial scar,
72 which is created locally by reactive astrocytes and astrocytes-secreted ECM molecules such as HA and
73 chondroitin sulphate proteoglycans (Bush et al., 1999; Lau et al., 2013).

74 We have previously demonstrated that high extracellular adenosine levels, a hallmark of ischemic
75 insults, induce astrogliogenesis from the SVZ (Benito-Muñoz et al., 2016). Following our previous
76 results, here we characterize the SVZ response to brain ischemia and investigate the role of newly
77 generated astrocytes in the modulation of the glial scar after MCAO. We show that ischemic conditions
78 increase the number of newly generated astrocytes in the SVZ and their migration to the ischemic area.
79 We also propose the role of these astrocytes in modulating the extracellular matrix at the glial scar and
80 suggest this astrocyte population as a possible target for brain repair after brain ischemia.

81

82 **RESULTS**

83 **Thbs4 is expressed in the neurogenic niche of the SVZ.**

84 As suggested by others (Benner et al., 2013; Girard et al., 2014; Pous et al., 2020), Thbs4 is highly
85 expressed in astrocytes of the SVZ and RMS and might play a role in ischemia-induced neurogenesis.
86 To confirm these observations, we labeled the mouse SVZ by immunofluorescence for Thbs4. Thbs4
87 was mainly expressed in the SVZ, RMS, and OB but also in the cerebellum and ventral tegmental area

88 (Fig. 1a). In the SVZ, the staining was associated with cells with different morphologies (Fig. 1b),
89 ranging from cells with small primary apical processes in contact with the ventricle, to rounded NSC-
90 like cells in the dorsolateral SVZ horn. After quantification by direct count of Thbs4-positive cells,
91 Thbs4-positive astrocytes represented 21.4% of the total SVZ cells (Fig. 1c), with more than 60% of
92 them displaying a radial glia-like type-B morphology (Bond et al., 2015; Doetsch et al., 1999) (Fig. 1d).
93 This is in accordance with other studies reporting Thbs4 expression in B-cells, either by
94 immunohistochemistry (Beckervordersandforth et al., 2010; Benner et al., 2013) or single-cell RNA
95 sequencing (Basak et al., 2018; Cebrian-Silla et al., 2021; Llorens-Bobadilla et al., 2015).

96 To validate the immunohistochemistry protocol for Thbs4, we labeled the SVZ cells with green
97 fluorescent protein (GFP) under the control of the Thbs4 promoter (pThbs4-eGFP) by postnatal (P1)
98 electroporation (Fig. 1e). Twenty-four hours after electroporation, almost 20% of total cells in the dorsal
99 SVZ expressed GFP (Fig. 1f), with a greater expression in the rostral SVZ (Fig. 1g), confirming that
100 Thbs4-positive cells were mainly localized in the neurogenic niche of the SVZ. This also suggests that
101 Thbs4 is expressed in NSCs at early postnatal stages, generating astrocytes during development.

102

103 **Thbs4 expression in the SVZ increases after brain ischemia**

104 To investigate whether brain ischemia could activate astrogliogenesis in the SVZ, we analyzed cell
105 proliferation and Thbs4 expression in the SVZ after MCAO. Sixty minutes of MCAO (Fig. S1a) caused
106 neuronal damage in the cortex and striatum, as observed by cresyl violet staining (Fig. S1b) and NeuN
107 immunofluorescence (Fig. S1c). The survival rate at 28 days post-lesion was around 50% (Fig. S1d).
108 Moreover, motor deficits and animal weight of ischemic mice were monitored every day after MCAO
109 for 30 days. Motor deficits improved overtime, while body weight dropped sharply the first three days
110 after MCAO and was partially restored at 30 dpi (Fig. S1e, f).

111 To study cell proliferation in the SVZ, we administered 50 mg/kg BrdU i.p. every two hours (three
112 doses in total) the day before MCAO (Fig. S2a). We observed an increase in the number of total SVZ

113 BrdU-positive cells 24h after MCAO (Fig. S2b, c). Ki67 immunofluorescence of SVZ wholemount
114 preparations (Fig. S2d) also revealed a more than tenfold increase of proliferative cells 24h after MCAO
115 (Fig. S2e). In addition, we observed a significant increase in cleaved Caspase3-positive cells 24h post-
116 lesion (Fig. S2f, g). These results suggest a fast and specific proliferative response in the ischemia-
117 induced SVZ.

118 We next analyzed Thbs4 staining in combination with Nestin, an NSC marker, and Doublecortin
119 (DCX), a marker of neuroblasts, before and after MCAO. The entire SVZ was analyzed in sham and
120 ischemic mice 7-, 15- and 30-days post-ischemia (dpi). The immunofluorescence analysis of the SVZ
121 (Fig. 2a) showed a transient decrease in Nestin and DCX-positive cells but an increase of Thbs4-positive
122 astrocytes up to 15 dpi (Fig. 2b-d) compared to sham animals. The increase of Thbs4 astrocytes was
123 also confirmed by Western blot analysis using SVZ homogenates (Fig. 2e, f), evidencing a 2-fold
124 increased expression of Thbs4 in the ischemic SVZ. Similarly to immunofluorescence, Western blot
125 also showed decreased Nestin protein levels at 15 dpi (Fig. 2g). These results demonstrate that Thbs4
126 expression in the SVZ increases after ischemia, coinciding with a decrease in neuroblast markers,
127 suggesting that the classical pro-neuroblast program of the SVZ is interrupted in favor of the generation
128 of astrocytes after ischemia.

129

130 **Characterization of ischemia-induced cell populations in the SVZ**

131 To characterize the different cell populations of the SVZ activated after focal ischemia, we labeled the
132 whole pool of proliferating cells with 1% BrdU in drinking water for 14 days before MCAO (Codega
133 et al., 2014). One month after MCAO, BrdU in the SVZ primarily stained slow proliferative cells like
134 type B cells, whereas in rapid transit-amplifying cells (type C), BrdU was diluted away. Therefore, we
135 chose to label type C cells by intraperitoneal administration (50 mg/kg) of 5-Iodo-2′-deoxyuridine (IdU)
136 24h before euthanasia (Fig. 3a). To identify the cellular origin of newborn astrocytes, we analyzed the
137 SVZ 30 dpi by immunofluorescence co-labeling Thbs4 and GFAP together with BrdU or IdU. We
138 found a 2-fold increase in the total amount of proliferative cells (BrdU-positive) after MCAO with

139 respect to the sham group (Fig. 3b), whereas we did not observe a significant change in the number of
140 IdU-positive cells (Fig. 3c). The number of slow proliferative NSC (Thbs4/GFAP/BrdU) increased
141 linearly after MCAO (Fig. 3d, e) especially in the dorsal region of the SVZ (Fig. S3a), whereas the
142 number of activated NSC (Thbs4/GFAP/IdU) did not change significantly, either in the whole SVZ
143 (Fig. 3f) or in any subregion analyzed (Fig. S3b). These results suggest that, after ischemia, Thbs4-
144 positive astrocytes derive from the slow proliferative type B cells.

145

146 **Ischemia-induced newborn astrocytes migrate from the dorsal SVZ to ischemic regions**

147 To confirm that Thbs4-positive astrocytes originate from type B cells of dorsal SVZ, we labeled NSCs
148 of dorsal SVZ by electroporating the pCAGGSx-CRE plasmid in P1 Ai14 Rosa26-CAG-tdTomato
149 transgenic mice (Fig. 4a). Plasmid electroporation induced the expression of tdTomato (tdTOM) by Cre
150 recombination, enabling the spatial tracking and cell fate assessment of electroporated NCSs from the
151 dorsal SVZ. Three to four months after electroporation, we performed the MCAO, and tdTOM
152 fluorescence was analyzed at 7, 30, and 60 dpi. To confirm the efficient labeling of NSCs by the
153 electroporation protocol, we followed the tdTOM fluorescence in the OB (Fig. S4a, see methods). Only
154 those animals with tdTOM-positive cells in the OB were taken into account for later analysis. After
155 quantification of tdTOM-positive NSCs 7, 30, and 60 dpi, we observed a significant decrease in tdTOM-
156 positive cells in ischemic animals in all SVZ regions analyzed (Fig. 4b, c and Fig S4b), suggesting that
157 they either left the area, or died. Conversely, there was a general increase of tdTOM-positive cells
158 outside the SVZ (Fig. 4d, e), especially in the intermediate and caudal axis of the whole brain compared
159 to sham animals (Fig. S4d-g), suggesting that electroporated cells had migrated away from the SVZ.

160 To identify the proportion of NSCs that differentiated into Thbs4-positive astrocytes following
161 ischemia, we analyzed the co-expression of Thbs4 with tdTOM after MCAO. Despite the general
162 decrease of tdTOM-positive cells in the SVZ, the fraction of Thbs4/tdTOM cells increased at 30 dpi
163 after MCAO (Fig. 4f, g), reaching a maximum increase at 60 dpi (Fig. 4h), in particular in rostral and
164 intermediate SVZ (Fig. S4c). Finally, we analyzed the Thbs4-positive astrocytes recruitment to the

165 ischemic regions. More than half of the total tdTOM-positive cells in the infarcted area expressed the
166 Thbs4 marker at 60 dpi (Fig. 4i, j). These results suggest that ischemia-induced astrogliogenesis in the
167 SVZ occurs in type B cells from the dorsal region and that these newborn Thbs4-positive astrocytes
168 migrate to the ischemic areas.

169

170 **Thbs4-positive astrocytes accumulate at the glial scar after brain ischemia.**

171 Besides its role in the neurogenic niches, Nestin is also rapidly and locally expressed by reactive
172 astrocytes and participates in glial scar formation (Frisén et al., 1995). Thus, we used Nestin
173 immunofluorescence as a reliable tool to identify the lesion border where the glial scar occurs (Fig. 5a).
174 Nestin staining of the scar was also compared with more classical methodologies like TTC staining
175 (Fig. 5b), where viable tissue is stained red and dead tissue is left unstained. The white-pale pink area
176 was then measured as infarct tissue by TTC staining (Fig. 5c). Unlike the TTC staining, which can only
177 be performed shortly after the lesion, the visualization of the glial scar with Nestin immunofluorescence
178 allowed us to analyze the lesion at later time-points. We observed a rapid formation of the glial scar as
179 early as 7 dpi (Fig. 5d). Analyzing the expression of the two astrocytic markers, Thbs4 and GFAP, as a
180 percentage of the glial scar region-of-interest (ROI), we observed different dynamics and localization.
181 GFAP expression increased rapidly after 7 days within the glial scar ROI, whereas Thbs4 was
182 upregulated at 15 dpi (Fig. 5e). This delay suggested that the glial scar harbors two different astrocytic
183 sub-populations: GFAP-only or GFAP/Thbs4. To analyze the spatial location of GFAP and Thbs4
184 markers within the Nestin border, we measured the fluorescence intensity profile of damaged area at 30
185 dpi. GFAP was found in both the scar and core areas, whereas Thbs4 fluorescence was found mostly at
186 the borders of the glial scar (Fig. 5f, g). Analysis and dynamics of Thbs4-positive astrocyte migration
187 were further performed in the corpus callosum (CC), striatum (Str), cortex (Ctx) and olfactory bulb
188 (OB) (Fig. S5a). We observed a linear increase of Thbs4-positive astrocytes from 7 to 60 dpi, both in
189 the Ctx and Str (Fig. S5b). Migration occurred mainly through the corpus callosum; among the total
190 GFAP-positive astrocytes, 36.5% were also positive for Thbs4, suggesting that more than one-third of

191 the astrocytes in the glial scar originated from the SVZ (Fig. S5c). Likewise, the number of DCX-
192 positive cells dramatically decreased 15 dpi in all OB layer (Fig. S5d-f) together with a significant
193 decrease of BrdU-positive cells (Fig. S5g) DCX/BrdU- positive neuroblasts in the RMS (Fig. S5h),
194 suggesting that ischemia induced a change in the neuroblasts' ectopic migratory pathway, depriving the
195 OB layers of SVZ newborn neurons.

196

197 **Thbs4-positive astrocytes modulate extracellular matrix homeostasis at the glial scar**

198 To investigate the role of Thbs4-positive astrocytes in the glial scar, we analyzed hyaluronic acid (HA),
199 the main component of the brain extracellular matrix (ECM), using the hyaluronic acid binding protein
200 (HABP) as a marker. Following ischemic damage, local astrocytes (GFAP+/Thbs4-) react by adopting
201 a fibrotic morphology, producing high-molecular weight HA (HMW-HA) to form the glial scar and
202 isolate the damaged area (Preston and Sherman, 2011). We then examined HA deposition in the corpus
203 callosum and the infarcted areas after MCAO. HABP immunofluorescence (Fig. 6a) and image analysis
204 revealed HA accumulation in the infarcted areas. Skeleton analysis, which quantifies the length of HA
205 chains and correlates with its molecular weight, identified progressively longer HA cable-like structures
206 at the glial scar as the infarct evolved (Fig. 6b). Fractal dimension analysis, which reflects the
207 interconnectivity of the extracellular matrix (Soria et al., 2020), further confirmed HA accumulation
208 and increased matrix complexity in infarcted areas, but not in corpus callosum (Fig. 6c), suggesting that
209 ECM accumulation is different in white and gray matter.

210 The proximity of Thbs4-positive astrocytes to HA in the ischemic scar (Fig. 6d, e) led us to investigate
211 if this population contributed to ECM production and, consequently, to scar formation. Since HA is
212 produced exclusively at the cell membrane (Sherman et al., 2015; Zimmermann and Dours-
213 Zimmermann, 2008), we analyzed HA labeling within 1 μm of the Thbs4-positive cell membrane in
214 high-resolution confocal images (Fig. 6f). Image analysis showed a significant increase in HABP area
215 at Thbs4-positive astrocyte-cell membranes after MCAO (Fig. 6g), suggesting a role of Thbs4-positive
216 astrocytes in HA production within the glial scar.

217 To explore the potential role of Thbs4-positive astrocytes in HA removal, we quantified intracellular
218 HABP spots in Thbs4-positive astrocytes at the glial scar. While HMW-HA cleavage occurs
219 extracellularly, HA fragments can be internalized for degradation by lysosomal hyaluronidases (Preston
220 and Sherman, 2011; Zimmermann and Dours-Zimmermann, 2008). Intracellular HABP spots were
221 compared between Thbs4-positive astrocytes and local astrocytes (GFAP-positive/Thbs4-negative)
222 (Fig. S6a). Thirty days after MCAO, Thbs4-positive astrocytes showed more intracellular HABP than
223 local astrocytes in the infarcted cortex (Fig. S6b). However, the number of HA spots internalized was
224 higher in local astrocytes compared with Thbs4 astrocytes (Fig. S6c), suggesting that Thbs4-positive
225 cells internalize HA in fewer vesicles. To confirm that astrocytes were degrading HA, we performed an
226 immunofluorescence analysis of CD44 (Fig. S6d). CD44 is a transmembrane glycoprotein receptor that
227 mediates HA internalization and degradation, and therefore ECM remodeling (Dzwonek and
228 Wilczynski, 2015). We detected that around 50% of the total Thbs4-positive astrocytes contained
229 internalized CD44 receptor, in the striatum 30 dpi (Fig. S6e), with higher numbers (60%) for the
230 infarcted corpus callosum. These findings suggest that Thbs4- positive astrocytes participate in both the
231 formation and degradation of the extracellular matrix at the glial scar.

232 To further investigate HA internalization by astrocytes, we conducted *in vitro* experiments using
233 cultures of rat SVZ neural stem cells, a more versatile preparation that displays the same HA
234 internalization and degradation machinery as mouse brain tissue (Sherman et al., 2015). An oxygen and
235 glucose deprivation (OGD) protocol was applied as an ischemia model and cells were fixed 7 days after
236 OGD (Fig. S7a). HA was analyzed via HABP immunofluorescence (Fig. S7b), both inside and outside
237 the Thbs4-positive cells (Fig. S7c). Thbs4-positive cells showed increased intracellular HA after OGD
238 (Fig. S7d), while extracellular HA levels decreased (Fig. S7e). However, this phenomenon was reversed
239 after adding hyaluronidases in the extracellular space (Fig. S7f, g), suggesting that Thbs4-positive cells
240 from SVZ homogenates can internalize or synthesize HA depending on external stimuli. HA
241 internalization was also measured in Iba1-positive cell cultures where we observed a reduced
242 internalization compare to Thbs4-positive cells (Fig. S7h). Lastly, metalloproteinase activity was found

243 to be increased in Thbs4 cultures following OGD (Fig. S7i). Altogether, these results suggest Thbs4-
244 positive cells can internalize HA after ischemic conditions but also synthetize it when ECM is degraded.

245

246 **Hyaluronan accumulation is sufficient but not exclusive for the recruitment of Thbs4-positive**
247 **astrocytes**

248 Since Thbs4-positive astrocytes migrate to the glial scar but not to the ischemic core, we hypothesized
249 that HA, the primary component of the ischemic scar, may be the trigger signal for recruiting Thbs4-
250 positive astrocytes. To test this hypothesis, we simulated the ECM accumulation that occurs at the scar
251 by overexpressing the Hyaluronan synthase 2 (HAS2) from the naked mole rat (*Heterocephalus glaber*),
252 a tool often used in mice to produces HA of very high molecular weight (Tian et al., 2013; Zhang et al.,
253 2023). We used a viral vector (AAV2/9-CAG-HAS2-3xFlag) with a FLAG tag to visualize transduced
254 cells after intracerebral inoculation in the striatum and checked HA accumulation in FLAG-positive
255 areas using HABP staining (Fig. 7a). We overexpressed HAS2 (or GFP as control) unilaterally. In a
256 subset of animals that underwent MCAO, AAV-HAS2 was injected contralateral to the infarct, to
257 compare Thbs4-positive astrocytes recruitment by both stimuli, the inflammation from the ischemic
258 damage and the HA accumulation *per se* (Fig. 7b). FLAG-positive cells were quantified as a surrogate
259 marker of viral infection for both control and MCAO groups (Fig. 7c). The GFP control group did not
260 increase HA production *per se* (Fig. 7d). However, HA overexpression was observed in HAS2 groups
261 (both control and MCAO group) by HABP immunofluorescence (Fig. 7e, f).

262 HA accumulation was sufficient to recruit the Thbs4-positive astrocytes from the ipsilateral SVZ 45
263 days after AAV-HAS2 inoculation (Fig. 7g), with a similar time window to that observed after MCAO.
264 Interestingly, when we induced a lesion by MCAO and performed viral overexpression of HAS2 in the
265 contralateral hemisphere, we found that Thbs4-positive astrocytes preferentially migrated to the
266 ischemic glial scar (Fig. 7g). This migration of Thbs4-positive astrocytes to the site of ischemic damage
267 occurred despite no differences in HA overexpression between contralateral (HAS2 infected) and
268 ipsilateral (infarcted area) hemispheres (Fig. 7h). These results suggest that the accumulation of HMW-

269 HA alone is sufficient to activate and recruit Thbs4-positive astrocytes from the SVZ. However, the
270 preferential migration to the ischemic scar indicates that brain ischemia generates a more potent
271 biochemical signal that not only activates the SVZ but also recruits newborn astrocytes.

272

273 **Ischemia-induced gliogenesis at the SVZ correlates with local hyaluronan degradation**

274 It is known that the niche microenvironment has a unique ECM composition (Kjell et al., 2020) and
275 that the stiffness of the niche plays a crucial role in the proliferation and differentiation of progenitor
276 cells (Long and Huttner, 2019; Segel et al., 2019). After observing the close association between Thbs4-
277 positive astrocytes and the ECM at the glial scar, we decided to study the Thbs4/HA tandem in the SVZ
278 following MCAO (Fig. 8a). We did not observe any significant changes in the HA area across the entire
279 SVZ but noted a decrease at 7 and 15 dpi in the dorsal SVZ (Fig. 8b-d). Skeleton analysis showed
280 fragmentation of HA exclusively in the dorsal SVZ at 7 and 15 dpi (Fig. 8e-g), i.e., earlier than the
281 migration of these newborn astrocytes toward the lesion.

282 Next, we examined the expression of genes related to HA degradation (*Hyase 1, 2* and *3*) and synthesis
283 (*HAS 1* and *HAS 2*). We also analyzed *Thbs4* and hypoxia-inducible factor 1-alpha (*Hif1a*), which are
284 known to be upregulated in the SVZ following brain ischemia (Benito-Muñoz et al., 2016; Liu et al.,
285 2007). Fresh SVZ tissue was collected from sham, 15 and 30 dpi mice (Fig. 8h). We observed an
286 increased expression of all Hyases at 15 dpi and slightly decreased by 30 dpi, whereas synthases (HAS)
287 showed a gradual increase from 15 to 30 dpi (Fig. 8i). Additionally, we observed an upregulation of
288 Thbs4 and Hif1a both at 15 and 30 dpi (Fig. 8i). These results suggest that HA degradation in the SVZ
289 is correlated with the Thbs4 response to ischemia.

290

291 **DISCUSSION**

292 The effects of brain insult on adult neurogenesis have been extensively discussed, both in animal models
293 and humans. However, whether these injuries can trigger the generation of newborn astrocytes from the
294 neurogenic niches remains a topic of debate. Neural stem cells in the adult brain are a remnant of
295 embryonic radial glia. Some researchers suggest that depletion of neurogenesis in the adult brain is a
296 consequence of astrogliogenesis (Encinas et al., 2011), while others propose astrogliogenesis is part of
297 a neurorestorative program originating from the neurogenic niches (Bonzano et al., 2018; Sohn et al.,
298 2015). Despite these differing perspectives, direct and definitive evidence of the generation of newborn
299 astrocytes from the SVZ or the SGZ has yet to be presented, as well as the potential role of these
300 astrocytes in aging and pathological conditions. In this study, we confirm that a strong and acute
301 damage-associated stimulus in the brain, such as an ischemic infarct, prompts astrogliogenesis in the
302 SVZ. Furthermore, we demonstrate that these astrocytes, which are positive for Thbs4, migrate to the
303 glial scar and play a role in its modulation, being capable of synthesis and degradation of hyaluronan,
304 a key component of the ECM at the scar.

305 Our findings align with previous studies, where cortical injury initiated by photothrombotic/ischemia
306 was shown to trigger a substantial production of Thbs4-positive astrocytes from the SVZ, a process
307 modulated by Notch activation (Benner et al., 2013). In this work, the authors suggested a clear role for
308 Thbs4-positive astrocytes in modulating the ischemic scar. In fact, homozygotic deletion of the Thbs4
309 gene led to abnormal glial scar formation and increased microvascular hemorrhage following brain
310 ischemia. Similarly, our results demonstrate that the adult neurogenic niche at the SVZ responds early
311 after ischemic stroke, degrading local hyaluronan plausibly to modify niche stiffness and facilitate
312 proliferation and differentiation of NSCs. Further experiments using Thbs4-knockout models will help
313 confirm this hypothesis.

314 By labeling NSC via *in vivo* postnatal electroporation, we provided proof of the origin and migration
315 of newborn Thbs4-positive astrocytes from the SVZ to the ischemic scar in response to the injury.
316 Notably, Thbs4 is expressed in the newborn astrocytes that migrate to the scar, whereas local reactive
317 astrocytes at the site of injury express only GFAP. It is likely that SVZ-derived newborn astrocytes

318 require Thbs4 expression to facilitate their migration to the ischemic area, as Thbs4 deletion has been
319 shown to impair migration of SVZ-derived cells along the RMS (Girard et al., 2014).

320 It is noteworthy that while the local, "GFAP-only", reactive astrocytes at the scar are capable of forming
321 the required ECM (Cregg et al., 2014; Wanner et al., 2013), we show that Thbs4-positive (Thbs4/GFAP)
322 astrocytes are also recruited from the SVZ to modulate scar formation. Unlike local reactive astrocytes,
323 which are hastily generated and present both at the core and periphery of the lesion, the newborn
324 astrocytes from the SVZ arrive later to the injury. We demonstrate that these Thbs4-positive astrocytes
325 migrate from the SVZ to the lesion and halt at the lesion border (precisely defined by Nestin staining),
326 establishing residence at the scar but not beyond.

327 The molecular signals that trigger gliogenesis in the SVZ and recruit newborn astrocytes to the lesion
328 remain unclear. We previously identified adenosine, a byproduct of ATP hydrolysis, as a strong
329 candidate, as it stimulates astrogliogenesis through A1 receptors following OGD *in vitro* and ischemia
330 *in vivo* (Benito-Muñoz et al., 2016). Here, we show that viral-mediated overproduction of HA, the
331 primary component of the glial scar, is sufficient to activate the generation and migration of the Thbs4-
332 positive astrocytes from the SVZ. Loss-of-function studies, using HA-depletion models or HA synthase
333 (Has)-deficient mice are still needed to corroborate this finding, although the inflammation associated
334 with HA deficiency might confound interpretation. Indeed, our results also show that the ischemic
335 infarct, with its proinflammatory (cytokines, chemokines) and proteolytic (MMPs, ROS) signals
336 (Jayaraj et al., 2019), serves as a more potent attractor than the ECM alone.

337 The glial response from the SVZ we propose in this study might have several functional implications.
338 Thbs4-positive astrocytes generated from the SVZ might act as a second wave of reactivity, supporting
339 local astrocytes in modulating ECM formation. Hyper-reactive astrocytes at the lesion border decrease
340 over time, along with reductions in HA synthesis and CD44 activity, suggesting that the second wave
341 of Thbs4-positive astrocytes from the SVZ could sustain high levels of HA production (Lindwall et al.,
342 2013). Thus, Thbs4-positive astrocytes may be crucial during this delayed temporal window when glial
343 scar remodeling is essential for neurological recovery (Cai et al., 2017; Dzyubenko et al., 2018).

However, it's important to note that only about one-third of the astrocytes at the glial scar are derived from the SVZ. This suggests that while SVZ-derived astrocytes may be important for glial scar maintenance, local astrocytes remain the central players in this process.

Based on our observations of both HA production and internalization by Thbs4-positive astrocytes *in vivo* within the ischemic region and *in vitro* following OGD, we propose a role for these astrocytes in the modulation, and possibly maintenance, of the ECM at the scar. It is likely that ECM degradation at the scar is also carried out by professional macrophages, such as microglia, which are known to be recruited to the scar (Fawcett and Asher, 1999) and have been shown to degrade ECM through phagocytosis (Nguyen et al., 2020; Soria et al., 2020). Understanding which cells within the scar environment participate in its modulation, particularly its degradation, holds highly therapeutic value for promoting regeneration (Dzyubenko et al., 2018; Silver and Miller, 2004). Here, we shed light on the unknown role of SVZ-derived astrocytes activated by ischemic brain injury and propose them as critical players in tissue regeneration after brain ischemia.

ACKNOWLEDGEMENTS

The authors thank Juan Carlos Chara, Zara Martínez-Paez, and Laura Escobar for their invaluable technical support. We thank Laura Simon for proofreading the manuscript, and Abraham Martín, Mónica Benito-Muñoz and Sol Beccari for training in MCAO in mice. We also thank Vera Gorbunova (University of Rochester, USA) for providing the cDNA of HAS2 from the naked mole rat. We thank Marie-Laure Thiolat and Dr. Nathalie Dutheil for AAV production. This study received financial support from the French government in the framework of the University of Bordeaux's IdEx "Investments for the Future" program/GPR BRAIN_2030 (B.D.). F.C. acknowledges funding from BIOEF (BIO21/COV/012), Eukampus, Plan Complementario en Salud (PRTR-C17.I1) and the Basque Government. F.N.S. was funded by the Spanish Research Agency (IJCI-2017-32114, PID2020-115896RJ-I00 and RYC2021-032602-I co-funded by NextGeneration EU/PRTR). C.M. acknowledges

funding from the Basque Government (IT1203-19) and CIBERNED. M.A. was supported by a PhD fellowship from the Basque Government.

AUTHOR CONTRIBUTIONS

M.A. conducted experiments and collected and analyzed data. M.C.T. and H.C. provided the Ai14-Rosa26-CAG-tdTomato$^{flx/flx}$ mice and technical input for electroporation. B.D. provided the AAV-HAS2 and conceived the idea of glial scar simulation. F.C., F.N.S. and C.M. secured funding. C.M. provided infrastructural support and scientific feedback. F.C. and F.N.S. conceived and supervised the study. F.P.C. supervised the study. M.A. and F.N.S. prepared the figures. M.A., F.N.S. and F.C. wrote the paper, with input from all authors.

380 **METHODS**

381 **Animals**

382 Male and female wild-type C57BL6/J mice and Ai14-Rosa26-CAG-tdTomato$^{flx/flx}$ transgenic mice bred
383 at the animal facility of UPV/EHU were used for *in vivo* experiments. Sprague Dawley rat pups from
384 P4 to P7 were used for *in vitro* experiments. All animals for *in vitro* and *in vivo* studies were handled
385 in accordance with the European Communities Council Directive (2010/63/EU). All possible efforts
386 were made to minimize animal suffering and the number of animals used. Animals were maintained
387 under standard laboratory conditions with food and water *ad libitum*.

388

389 **Transient MCAO**

390 Brain ischemia was induced in 3-4-month old C57BL/6 mice (approximately 25 g) by occluding 60
391 minutes of the lenticulo-striate arteries with a 10 mm length of silicone-coated 6-0 monofilament nylon
392 suture (602223PK10, Doccol Corporation) using a modification of the protocol described by
393 (Gelderblom et al., 2009). Arteries occlusion generated a specific lesion in the cortex and striatum that
394 was evaluated at different times after the MCAO (7, 15, 30 or 60 days after occlusion). Ischemic damage
395 was evaluated in the ipsilateral hemisphere by Cresyl violet staining, Nestin immunofluorescence or
396 hyaluronan staining. Sham animals, in which arteries were visualized but not disturbed, were used as
397 an experimental control. Both experimental groups, sham and ischemic, were anesthetized with a mix
398 of isoflurane and oxygen (induction of anesthesia with 4% isoflurane and maintenance for surgery at
399 1.5% isoflurane) and maintained under analgesia with buprenorphine 24 hours after ischemia (0.03
400 mg/Kg body weight i.p. every 12h). Animal wellness was evaluated daily, controlling the body weight
401 and the motor deficit of the animal by means of neurological scores and pole test. Motor deficit was
402 assessed in each animal 1h after MCAO and later every 24h. Animals without neurological deficits
403 were excluded from the study.

404

405 **5-bromo-2'-deoxyuridine (BrdU) protocol**

406 The total pool of proliferating cells was labelled with three injections of 50 mg/kg 5-bromo-2'-
407 deoxyuridine (BrdU) the day before MCAO protocol. Animals were sacrificed the day after MCAO to
408 analyse acute SVZ proliferation. Chronic BrdU protocol was performed for quiescent NSC
409 identification (Codega et al., 2014). Briefly, 1% of BrdU was administered in the drinking water for 14
410 days. On day 15, BrdU was removed and animals were subjected to MCAO protocol. Mice were
411 sacrificed and perfused at 3, 7, 15, and 30 days after MCAO, although only animals with a temporal
412 window of 30 days between MCAO and perfusion were used for statistical analysis. Activated cells
413 were labelled by i.p. injection of 50 mg/Kg 5-iodo-2′-deoxyuridine (IdU) 24 hours before euthanasia.

414

415 **Electroporation**

416 Ai14-Rosa26-CAG-tdTomato$^{flx/flx}$ transgenic mice and pCAGGS-CRE plasmid were kindly provided
417 for Prof. Harold Cremer and Marie-Catherine Tiveron from Institut de Biologie du Développement de
418 Marseille (IBDM). Postnatal electroporation was performed as described previously (Platel et al., 2019).
419 Mice pups from P0-P2 were anesthetized by hypothermia. pCAGGS-CRE plasmid was used at a final
420 concentration of 2.5 µg/ul and 2µl was injected in the lateral ventricle by expiratory pressure using a
421 glass micropipette. Following injection, pup brains were placed between electrodes targeted the dorsal
422 SVZ and subjected to five 95V electrical pulses (50 ms, 950 ms intervals). BTX ECM399 (Thermo
423 Fisher Scientific) electroporator was used with 7 mm tweezer electrodes. Electroporated pups were
424 reanimated at 37ºC before returning to the mother.

425 In order to analyze the Thbs4 positive cells in the SVZ, we subcloned the eGFP gene (from a pCMV-
426 eGFP N1) into a PGL3-basic backbone containing mouse Thbs4 promoter, kindly provided by Stenina-
427 Adognravi lab (Muppala et al., 2017). pThbs4-GFP was also electroporated in P0-P2 mice, and
428 euthanized 1-day post-electroporation to corroborate Thbs4 expression in the SVZ at postnatal stages.

429

430 **AAV vector production**

431 AAV2/9-CAG-HAS2-3xFlag vector was produced by polyethylenimine (PEI) mediated triple
432 transfection of low passage HEK-293 T/17 cells (ATCC; cat number CRL-11268). The respective AAV
433 expression plasmid expression plasmid pNMRHAS2_N1 (provided by Dr. Vera Gorbunova) was
434 cotransfected with the adeno helper pAd Delta F6 plasmid (Penn Vector Core, cat # PL-F-PVADF6)
435 and AAV Rep Cap pAAV2/9 plasmid (Penn Vector Core, cat # PL-TPV008). AAV vector was purified
436 as previously described (Bourdenx et al., 2015). Cells are harvested 72 h post-transfection, resuspended
437 in lysis buffer (150 mM NaCl, 50 mM Tris–HCl pH 8.5) and lysed by 3 freeze-thaw cycles (37°C/-
438 80°C). The cell lysate is treated with 150 units/ml Benzonase (Sigma, St Louis, MO) for 1 h at 37°C,
439 and the crude lysate is clarified by centrifugation. Vectors are purified by iodixanol step gradient
440 centrifugation and concentrated and buffer-exchanged into Lactated Ringer's solution (Baxter,
441 Deerfield, IL) using vivaspin20 100 kDa cut-off concentrator (Sartorius Stedim, Goettingen, Germany).
442 Titrations were performed at the transcriptome core facility (Neurocentre Magendie, INSERM U862,
443 Bordeaux, France). The genome-containing particle (gcp) titer was determined at a concentration of
444 1.10^{13} gcp/ml by quantitative real-time PCR using the Light Cycler 480 SYBR green master mix
445 (Roche, cat # 04887352001) with primers specific for the AAV2 ITRs (fwd 50-
446 GGAACCCCTAGTGATG GAGTT-3'; rev 50-CGGCCTCAGTGAGCGA-30) on a Light Cycler 480
447 instrument. The purity assessment of vector stocks was estimated by loading 10 µl of vector stock on
448 10 % SDS acrylamide gels; total proteins were visualized using the Krypton Infrared Protein Stain
449 according to the manufacturer's instructions (Life Technologies).

450

451 ***In vivo* AAV-HAS2 injections**

452 Mice were anesthetized with isoflurane and fixed to a stereotaxic frame connected with a gas mask. We
453 injected 1µl of adeno-associated virus (AAV2/9) CAG-HAS2-3xFlag (1x10^13 gc/µl) in the
454 contralateral striatum (AP: +1.0; ML: -1.8; DV: -3.2) to simulate scar tissue hyaluronan. After two
455 weeks, the ischemic group was subjected to the MCAO model in the ipsilateral hemisphere and perfused

456 30 days later. Only slices with representative lesions in both hemispheres were used for image and
457 statistical analysis.

458

459 **Immunofluorescence**

460 Mice were anesthetized with an intraperitoneal injection of pentobarbital (100 mg/kg). Brain tissues
461 were fixed by intracardiac perfusion using 4% paraformaldehyde. Fixed brains were sliced at 40 µm of
462 thickness using the Leica VT1200S vibratome (Leica Microsystems) and subjected to
463 immunofluorescence. For standard immunofluorescence protocol, tissue slices were permeabilized with
464 0.1% Triton and non-specific epitopes blocked with 1% Bovine Serum Albumin and 10% Donkey
465 serum in PBS. Primary antibodies (Supplementary Table 1) were incubated at different concentrations
466 (see Table 1 for specification) overnight at 4ºC and then washed three times with 0.1% Triton in PBS.
467 Secondary conjugated antibodies were incubated for 1 h at room temperature. After three washes with
468 0.1% Triton in PBS, cells were stained for 10 min with DAPI and further washed with PBS. Finally,
469 coverslips were mounted with Fluoromount (SouthernBiotech) and analyzed by fluorescence using the
470 confocal microscope Leica TCS SP8. For hyaluronic acid labeling, endogenous biotins were pre-
471 blocked using Streptavidin/Biotin blocking solution (Vector Labs, #SP-2002) following the
472 manufacturer's instructions and further blocked with PBS 1X 0.1% Saponin 1% BSA for one hour at
473 room temperature. Primary antibodies and biotinylated Hyaluronic Acid Binding Protein (HABP,
474 #385911 Millipore) were incubated for 72 hours at 4°C or 24 hours at room temperature. After three
475 washes with PBS, 1X 0.1% Saponin, secondary antibody and DAPI diluted in the same blocking buffer
476 were incubated for one hour at room temperature. Slices were mounted with Mowiol (Millipore
477 #475904) in superfrost slides (Thermo Fisher Scientific) and #1.5 coverslips.

478

479 **Imaging and image analysis**

480 Confocal images were acquired in a Leica TCS SP8 with 20x (0.8 NA) and 63x objectives (1.4 NA).
481 Images were taken with a pixel size of 90 nm. Widefield imaging was performed in a Zeiss AxioVision
482 fluorescence microscope and a 3DHISTECH panoramic MIDI II digital slide scanner. Settings were
483 adjusted for each individual experiment and kept for all conditions. Image processing was performed
484 using FIJI (Schindelin et al., 2012), CaseViewer and Hyugens (SVI, The Netherlands) software. For
485 Thbs4, Nestin and DCX immunofluorescence, wholemount SVZ preparations and AAV-HAS2
486 analysis, tile-scan was done using the navigator plug-in in the LasX software. For Nestin
487 immunofluorescence, images were deconvoluted using the Hyugens software.

488 SVZ images were reconstructed using the tile-scan tool (LasX software, Leica). SVZ region of interest
489 (ROI) was delimited manually and expression of each marker was measured in the SVZ ROI.
490 Quantification of all markers was done manually, except for HABP quantification, which was done
491 with custom FIJI scripts for in vitro (https://github.com/MariArdaya/Hyaluronan_v2) and in vivo
492 analysis (https://github.com/SoriaFN/Tools). The HABP signal was segmented with an automatic
493 threshold and colocalized with other markers such as CD44. This, combined with cell segmentation,
494 based on the Thbs4 mask, allowed for quantification of HABP area and number of spots inside cells,
495 outside cells or at the membrane (with a band ROI of 1 μm). The Analyze Skeleton and Fractal count
496 plugins were used on the skeletonized segmented HABP to quantify the longest shortest path and the
497 fractal dimension, respectively, to reveal the length and interconnectivity of the matrix network (Casey
498 et al., 2024; Soria et al., 2020).

499

500 **Western blot**

501 The SVZ was freshly dissected on ice and minced using a micro grinder. Total protein was extracted
502 after tissue lysis with RIPA buffer (Thermo Fisher Scientific #89900) and Protease and Phosphatase
503 Inhibitor Cocktail 100X (Thermo Fisher Scientific). Samples were lysed in ice for 10 minutes and
504 sonicated using an Ultrasonic Processor (Hielscher Ultrasound Technology). Sonicated tissues were
505 centrifuged at 1200 rpm for 10 min and 4°C to remove insoluble fragments. Protein concentration was

506 measured by chemioluminescence using RC DC™ Protein Assay (Bio-Rad). Forty micrograms of
507 protein samples were denatured in reducing loading buffer containing β-mercaptoethanol (M3148,
508 Sigma) and 0.0002% bromophenol blue at 95°C for 5 minutes and separated in pre-casted 12% or 7.5%
509 Tris-Glycine polyacrylamide gel using the Criterion cell system (Biorad). Electrophoresis was
510 conducted at 80 V in a Tris-Glycine buffer (25 mM Tris, 192 mM glycine, 0.1% SDS in dH2O, pH 8.3).
511 After complete separation, proteins were transferred to a nitrocellulose membrane (Biorad) using Trans-
512 Blot® TurboTM Transfer System (Bio-Rad). Nitrocellulose membranes were incubated in blocking
513 solution (Tris-Buffer Solution (TBS), 0.1% Tween-20 and 5% BSA) for one hour at room temperature.
514 Primary antibodies were incubated overnight at 4°C. Horseradish peroxidase-conjugated secondary
515 antibodies were incubated in blocking buffer for one hour at room temperature. Immunodetection was
516 performed by electrochemical luminescence in a Chemidoc MP (Biorad) and the intensity of the bands
517 was quantified using ImageLab (Bio-Rad) software corrected by Gaussian curves.

518

519 **qRT-PCR**

520 Fresh SVZ tissue from ipsilateral hemisphere was isolated as previously described from sham, 15 and
521 30 days after MCAO animals to analyze the expression of several genes (Supplementary Table 2). After
522 mechanical trituration, RNA was extracted from the tissue after mechanical trituration following the
523 manufacturer´s protocol (NZYTECH Total RNA Isolation kit protocol (NZYTECH, MB13402). RNA
524 concentration was measured by spectrophotometry using the Nanodrop 2000c spectrophotometer
525 (Thermo-Scientific, USA). Real time polymerase chain reaction (RT-PCR) from 10 ng of RNA was
526 performed using the One-step NZYTECH RT-qPCR Green kit according to manufacturer´s protocol
527 (NZYTECH, MB34302). RT-PCR was normalized using the housekeeping genes hypoxanthine
528 phosphoribosyl-transferase 1 (HPRT1, Qiagen QuantiTect Primer Assay, Barcelona, Spain). Specificity
529 of each amplification was confirmed by melting curve analysis. PCR reactions were performed in a
530 CFX96 Detection System (BioRad, Madrid, Spain). Semi-quantification was performed using the 2-

531 ΔΔCt algorithm. Unsupervised hierarchical distance matrix and distance matrix map was developed
532 using Orange3 software (Python v3.0).

533

534 **Statistical analysis**

535 Statistical analysis was done using GraphPad Prism software (version 8.0; GraphPad software). Data
536 are presented as mean ± SEM unless specified otherwise. Statistical analysis was performed using
537 unpaired Student´s t-test for independent conditions and paired Student´s t-test for dependent
538 conditions. In addition, one-way and two-way ANOVA were also performed to compare more than 2
539 groups among them. Tukey and Dunnett post-hoc tests were used. For HABP skeleton analysis,
540 Kruskal-Wallis analysis was performed to compare cumulative frequency curves in more than 2 groups.
541 *P* value was considered significant at $p < 0.05$. Sample number (*n*), *p* values and statistical test are
542 indicated in figure legends.

543

544 **REFERENCES**

545 Adams KL, Gallo V. 2018. The diversity and disparity of the glial scar. *Nat Neurosci* **21**:9–15.
546 doi:10.1038/s41593-017-0033-9
547 Anderson MA, Burda JE, Ren Y, Ao Y, O'Shea TM, Kawaguchi R, Coppola G, Khakh BS, Deming TJ,
548 Sofroniew MV. 2016. Astrocyte scar formation aids central nervous system axon
549 regeneration. *Nature* **532**:195–200. doi:10.1038/nature17623
550 Arvidsson A, Collin T, Kirik D, Kokaia Z, Lindvall O. 2002. Neuronal replacement from endogenous
551 precursors in the adult brain after stroke. *Nat Med* **8**:963–970. doi:10.1038/nm747
552 Basak O, Krieger TG, Muraro MJ, Wiebrands K, Stange DE, Frias-Aldeguer J, Rivron NC, van de
553 Wetering M, van Es JH, van Oudenaarden A, Simons BD, Clevers H. 2018. Troy+ brain stem
554 cells cycle through quiescence and regulate their number by sensing niche occupancy. *Proc*
555 *Natl Acad Sci U S A* **115**:E610–E619. doi:10.1073/pnas.1715911114
556 Beckervordersandforth R, Tripathi P, Ninkovic J, Bayam E, Lepier A, Stempfhuber B, Kirchhoff F,
557 Hirrlinger J, Haslinger A, Lie DC, Beckers J, Yoder B, Irmler M, Götz M. 2010. In vivo fate
558 mapping and expression analysis reveals molecular hallmarks of prospectively isolated adult
559 neural stem cells. *Cell Stem Cell* **7**:744–758. doi:10.1016/j.stem.2010.11.017
560 Benito-Muñoz M, Matute C, Cavaliere F. 2016. Adenosine A1 receptor inhibits postnatal
561 neurogenesis and sustains astrogliogenesis from the subventricular zone. *Glia* **64**:1465–
562 1478. doi:10.1002/glia.23010
563 Benner EJ, Luciano D, Jo R, Abdi K, Paez-Gonzalez P, Sheng H, Warner DS, Liu C, Eroglu C, Kuo CT.
564 2013. Protective astrogenesis from the SVZ niche after injury is controlled by Notch
565 modulator Thbs4. *Nature* **497**:369–373. doi:10.1038/nature12069

566 Bond AM, Ming G-L, Song H. 2015. Adult Mammalian Neural Stem Cells and Neurogenesis: Five
567 Decades Later. *Cell Stem Cell* **17**:385–395. doi:10.1016/j.stem.2015.09.003
568 Bonzano S, Crisci I, Podlesny-Drabiniok A, Rolando C, Krezel W, Studer M, De Marchis S. 2018.
569 Neuron-Astroglia Cell Fate Decision in the Adult Mouse Hippocampal Neurogenic Niche Is
570 Cell-Intrinsically Controlled by COUP-TFI In Vivo. *Cell Rep* **24**:329–341.
571 doi:10.1016/j.celrep.2018.06.044
572 Bourdenx M, Dovero S, Engeln M, Bido S, Bastide MF, Dutheil N, Vollenweider I, Baud L, Piron C,
573 Grouthier V, Boraud T, Porras G, Li Q, Baekelandt V, Scheller D, Michel A, Fernagut P-O,
574 Georges F, Courtine G, Bezard E, Dehay B. 2015. Lack of additive role of ageing in
575 nigrostriatal neurodegeneration triggered by α-synuclein overexpression. *Acta Neuropathol*
576 *Commun* **3**:46. doi:10.1186/s40478-015-0222-2
577 Bush TG, Puvanachandra N, Horner CH, Polito A, Ostenfeld T, Svendsen CN, Mucke L, Johnson MH,
578 Sofroniew MV. 1999. Leukocyte infiltration, neuronal degeneration, and neurite outgrowth
579 after ablation of scar-forming, reactive astrocytes in adult transgenic mice. *Neuron* **23**:297–
580 308. doi:10.1016/s0896-6273(00)80781-3
581 Cai H, Ma Y, Jiang L, Mu Z, Jiang Z, Chen X, Wang Y, Yang G-Y, Zhang Z. 2017. Hypoxia Response
582 Element-Regulated MMP-9 Promotes Neurological Recovery via Glial Scar Degradation and
583 Angiogenesis in Delayed Stroke. *Molecular Therapy* **25**:1448–1459.
584 doi:10.1016/j.ymthe.2017.03.020
585 Casey DT, Lahue KG, Mori V, Herrmann J, Hall JK, Suki B, Janssen-Heininger YMW, Bates JHT. 2024.
586 Local fractal dimension of collagen detects increased spatial complexity in fibrosis.
587 *Histochem Cell Biol* **161**:29–42. doi:10.1007/s00418-023-02248-8
588 Cavaliere F, Dinkel K, Reymann K. 2006. The subventricular zone releases factors which can be
589 protective in oxygen/glucose deprivation-induced cortical damage: an organotypic study.
590 *Exp Neurol* **201**:66–74. doi:10.1016/j.expneurol.2006.03.020
591 Ceanga M, Dahab M, Witte OW, Keiner S. 2021. Adult Neurogenesis and Stroke: A Tale of Two
592 Neurogenic Niches. *Frontiers in Neuroscience* **15**.
593 Cebrian-Silla A, Nascimento MA, Redmond SA, Mansky B, Wu D, Obernier K, Romero Rodriguez R,
594 Gonzalez-Granero S, García-Verdugo JM, Lim DA, Álvarez-Buylla A. 2021. Single-cell analysis
595 of the ventricular-subventricular zone reveals signatures of dorsal and ventral adult
596 neurogenesis. *eLife* **10**:e67436. doi:10.7554/eLife.67436
597 Chaker Z, Codega P, Doetsch F. 2016. A mosaic world: puzzles revealed by adult neural stem cell
598 heterogeneity. *WIREs Developmental Biology* **5**:640–658. doi:10.1002/wdev.248
599 Codega P, Silva-Vargas V, Paul A, Maldonado-Soto AR, DeLeo AM, Pastrana E, Doetsch F. 2014.
600 Prospective Identification and Purification of Quiescent Adult Neural Stem Cells from Their In
601 Vivo Niche. *Neuron* **82**:545–559. doi:10.1016/j.neuron.2014.02.039
602 Cregg JM, DePaul MA, Filous AR, Lang BT, Tran A, Silver J. 2014. Functional regeneration beyond the
603 glial scar. *Exp Neurol* **253**:197–207. doi:10.1016/j.expneurol.2013.12.024
604 Doetsch F, Caillé I, Lim DA, García-Verdugo JM, Alvarez-Buylla A. 1999. Subventricular zone
605 astrocytes are neural stem cells in the adult mammalian brain. *Cell* **97**:703–716.
606 doi:10.1016/s0092-8674(00)80783-7
607 Dzwonek J, Wilczynski GM. 2015. CD44: molecular interactions, signaling and functions in the
608 nervous system. *Front Cell Neurosci* **9**:175. doi:10.3389/fncel.2015.00175
609 Dzyubenko E, Manrique-Castano D, Kleinschnitz C, Faissner A, Hermann DM. 2018. Role of immune
610 responses for extracellular matrix remodeling in the ischemic brain. *Ther Adv Neurol Disord*
611 **11**:1756286418818092. doi:10.1177/1756286418818092
612 Encinas JM, Michurina TV, Peunova N, Park J-H, Tordo J, Peterson DA, Fishell G, Koulakov A,
613 Enikolopov G. 2011. Division-coupled astrocytic differentiation and age-related depletion of
614 neural stem cells in the adult hippocampus. *Cell Stem Cell* **8**:566–579.
615 doi:10.1016/j.stem.2011.03.010

616 Faulkner JR, Herrmann JE, Woo MJ, Tansey KE, Doan NB, Sofroniew MV. 2004. Reactive astrocytes
617 protect tissue and preserve function after spinal cord injury. *J Neurosci* **24**:2143–2155.
618 doi:10.1523/JNEUROSCI.3547-03.2004
619 Fawcett JW. 2015. The extracellular matrix in plasticity and regeneration after CNS injury and
620 neurodegenerative disease. *Prog Brain Res* **218**:213–226. doi:10.1016/bs.pbr.2015.02.001
621 Fawcett JW, Asher RA. 1999. The glial scar and central nervous system repair. *Brain Res Bull* **49**:377–
622 391. doi:10.1016/s0361-9230(99)00072-6
623 Frisén J, Johansson CB, Török C, Risling M, Lendahl U. 1995. Rapid, widespread, and longlasting
624 induction of nestin contributes to the generation of glial scar tissue after CNS injury. *Journal
625 of Cell Biology* **131**:453–464. doi:10.1083/jcb.131.2.453
626 Gelderblom M, Leypoldt F, Steinbach K, Behrens D, Choe C-U, Siler DA, Arumugam TV, Orthey E,
627 Gerloff C, Tolosa E, Magnus T. 2009. Temporal and spatial dynamics of cerebral immune cell
628 accumulation in stroke. *Stroke* **40**:1849–1857. doi:10.1161/STROKEAHA.108.534503
629 Girard F, Eichenberger S, Celio MR. 2014. Thrombospondin 4 deficiency in mouse impairs neuronal
630 migration in the early postnatal and adult brain. *Molecular and Cellular Neuroscience*
631 **61**:176–186. doi:10.1016/j.mcn.2014.06.010
632 Jayaraj RL, Azimullah S, Beiram R, Jalal FY, Rosenberg GA. 2019. Neuroinflammation: friend and foe
633 for ischemic stroke. *J Neuroinflammation* **16**:142. doi:10.1186/s12974-019-1516-2
634 Kjell J, Fischer-Sternjak J, Thompson AJ, Friess C, Sticco MJ, Salinas F, Cox J, Martinelli DC, Ninkovic J,
635 Franze K, Schiller HB, Götz M. 2020. Defining the Adult Neural Stem Cell Niche Proteome
636 Identifies Key Regulators of Adult Neurogenesis. *Cell Stem Cell* **26**:277-293.e8. doi:10/ghcp5v
637 Kralic JE, Ledergerber DA, Fritschy J-M. 2005. Disruption of the neurogenic potential of the dentate
638 gyrus in a mouse model of temporal lobe epilepsy with focal seizures. *European Journal of
639 Neuroscience* **22**:1916–1927. doi:10.1111/j.1460-9568.2005.04386.x
640 Lau LW, Cua R, Keough MB, Haylock-Jacobs S, Yong VW. 2013. Pathophysiology of the brain
641 extracellular matrix: a new target for remyelination. *Nat Rev Neurosci* **14**:722–729.
642 doi:10/f5b6w9
643 Laug D, Huang T-W, Huerta NAB, Huang AY-S, Sardar D, Ortiz-Guzman J, Carlson JC, Arenkiel BR, Kuo
644 CT, Mohila CA, Glasgow SM, Lee HK, Deneen B. 2019. Nuclear factor I-A regulates diverse
645 reactive astrocyte responses after CNS injury. *J Clin Invest* **129**:4408–4418.
646 doi:10.1172/JCI127492
647 Li L, Harms KM, Ventura PB, Lagace DC, Eisch AJ, Cunningham LA. 2010. Focal cerebral ischemia
648 induces a multilineage cytogenic response from adult subventricular zone that is
649 predominantly gliogenic. *Glia* **58**:1610–1619. doi:10.1002/glia.21033
650 Lindwall C, Olsson M, Osman AM, Kuhn HG, Curtis MA. 2013. Selective expression of hyaluronan and
651 receptor for hyaluronan mediated motility (Rhamm) in the adult mouse subventricular zone
652 and rostral migratory stream and in ischemic cortex. *Brain Res* **1503**:62–77.
653 doi:10.1016/j.brainres.2013.01.045
654 Liu XS, Zhang ZG, Zhang RL, Gregg S, Morris DC, Wang Y, Chopp M. 2007. Stroke induces gene profile
655 changes associated with neurogenesis and angiogenesis in adult subventricular zone
656 progenitor cells. *J Cereb Blood Flow Metab* **27**:564–574. doi:10.1038/sj.jcbfm.9600371
657 Llorens-Bobadilla E, Zhao S, Baser A, Saiz-Castro G, Zwadlo K, Martin-Villalba A. 2015. Single-Cell
658 Transcriptomics Reveals a Population of Dormant Neural Stem Cells that Become Activated
659 upon Brain Injury. *Cell Stem Cell* **17**:329–340. doi:10.1016/j.stem.2015.07.002
660 Long KR, Huttner WB. 2019. How the extracellular matrix shapes neural development. *Open Biol*
661 **9**:180216. doi:10/ghn8hs
662 Luskin MB. 1993. Restricted proliferation and migration of postnatally generated neurons derived
663 from the forebrain subventricular zone. *Neuron* **11**:173–189. doi:10.1016/0896-
664 6273(93)90281-u

Muppala S, Xiao R, Krukovets I, Verbovetsky D, Yendamuri R, Habib N, Raman P, Plow E, Stenina-Adognravi O. 2017. Thrombospondin-4 mediates TGF-β-induced angiogenesis. *Oncogene* **36**:5189–5198. doi:10.1038/onc.2017.140

Nguyen PT, Dorman LC, Pan S, Vainchtein ID, Han RT, Nakao-Inoue H, Taloma SE, Barron JJ, Molofsky AB, Kheirbek MA, Molofsky AV. 2020. Microglial Remodeling of the Extracellular Matrix Promotes Synapse Plasticity. *Cell* **182**:388-403.e15. doi:10/gg5cj3

Platel J-C, Angelova A, Bugeon S, Wallace J, Ganay T, Chudotvorova I, Deloulme J-C, Béclin C, Tiveron M-C, Coré N, Murthy VN, Cremer H. 2019. Neuronal integration in the adult mouse olfactory bulb is a non-selective addition process. *eLife* **8**:e44830. doi:10.7554/eLife.44830

Pous L, Deshpande SS, Nath S, Mezey S, Malik SC, Schildge S, Bohrer C, Topp K, Pfeifer D, Fernández-Klett F, Doostkam S, Galanakis DK, Taylor V, Akassoglou K, Schachtrup C. 2020. Fibrinogen induces neural stem cell differentiation into astrocytes in the subventricular zone via BMP signaling. *Nat Commun* **11**:630. doi:10.1038/s41467-020-14466-y

Preston M, Sherman LS. 2011. Neural Stem Cell Niches: Critical Roles for the Hyaluronan-Based Extracellular Matrix in Neural Stem Cell Proliferation and Differentiation. *Front Biosci (Schol Ed)* **3**:1165–1179.

Schindelin J, Arganda-Carreras I, Frise E, Kaynig V, Longair M, Pietzsch T, Preibisch S, Rueden C, Saalfeld S, Schmid B, Tinevez J-Y, White DJ, Hartenstein V, Eliceiri K, Tomancak P, Cardona A. 2012. Fiji: an open-source platform for biological-image analysis. *Nat Methods* **9**:676–682. doi:10/f34d7c

Segel M, Neumann B, Hill MFE, Weber IP, Viscomi C, Zhao C, Young A, Agley CC, Thompson AJ, Gonzalez GA, Sharma A, Holmqvist S, Rowitch DH, Franze K, Franklin RJM, Chalut KJ. 2019. Niche stiffness underlies the ageing of central nervous system progenitor cells. *Nature* **573**:130–134. doi:10/gf6j83

Sherman LS, Matsumoto S, Su W, Srivastava T, Back SA. 2015. Hyaluronan Synthesis, Catabolism, and Signaling in Neurodegenerative Diseases. *International Journal of Cell Biology* **2015**:e368584. doi:10/gccgm9

Silver J, Miller JH. 2004. Regeneration beyond the glial scar. *Nat Rev Neurosci* **5**:146–156. doi:10.1038/nrn1326

Sohn J, Orosco L, Guo F, Chung S-H, Bannerman P, Mills Ko E, Zarbalis K, Deng W, Pleasure D. 2015. The subventricular zone continues to generate corpus callosum and rostral migratory stream astroglia in normal adult mice. *J Neurosci* **35**:3756–3763. doi:10.1523/JNEUROSCI.3454-14.2015

Soria FN, Paviolo C, Doudnikoff E, Arotcarena M-L, Lee A, Danné N, Mandal AK, Gosset P, Dehay B, Groc L, Cognet L, Bezard E. 2020. Synucleinopathy alters nanoscale organization and diffusion in the brain extracellular space through hyaluronan remodeling. *Nat Commun* **11**:3440. doi:10.1038/s41467-020-17328-9

Sundholm-Peters NL, Yang HKC, Goings GE, Walker AS, Szele FG. 2005. Subventricular Zone Neuroblasts Emigrate Toward Cortical Lesions. *Journal of Neuropathology & Experimental Neurology* **64**:1089–1100. doi:10.1097/01.jnen.0000190066.13312.8f

Tian X, Azpurua J, Hine C, Vaidya A, Myakishev-Rempel M, Ablaeva J, Mao Z, Nevo E, Gorbunova V, Seluanov A. 2013. High-molecular-mass hyaluronan mediates the cancer resistance of the naked mole rat. *Nature* **499**:346–349. doi:10/ghcp25

Wanner IB, Anderson MA, Song B, Levine J, Fernandez A, Gray-Thompson Z, Ao Y, Sofroniew MV. 2013. Glial scar borders are formed by newly proliferated, elongated astrocytes that interact to corral inflammatory and fibrotic cells via STAT3-dependent mechanisms after spinal cord injury. *J Neurosci* **33**:12870–12886. doi:10.1523/JNEUROSCI.2121-13.2013

Yamashita T, Ninomiya M, Hernández Acosta P, García-Verdugo JM, Sunabori T, Sakaguchi M, Adachi K, Kojima T, Hirota Y, Kawase T, Araki N, Abe K, Okano H, Sawamoto K. 2006. Subventricular zone-derived neuroblasts migrate and differentiate into mature neurons in the post-stroke adult striatum. *J Neurosci* **26**:6627–6636. doi:10.1523/JNEUROSCI.0149-06.2006

716 Zhang Z, Tian X, Lu JY, Boit K, Ablaeva J, Zakusilo FT, Emmrich S, Firsanov D, Rydkina E, Biashad SA, Lu
717 Q, Tyshkovskiy A, Gladyshev VN, Horvath S, Seluanov A, Gorbunova V. 2023. Increased
718 hyaluronan by naked mole-rat Has2 improves healthspan in mice. *Nature*.
719 doi:10.1038/s41586-023-06463-0
720 Zimmermann DR, Dours-Zimmermann MT. 2008. Extracellular matrix of the central nervous system:
721 from neglect to challenge. *Histochem Cell Biol* **130**:635–653. doi:10.1007/s00418-008-0485-9
722

723 **FIGURES**

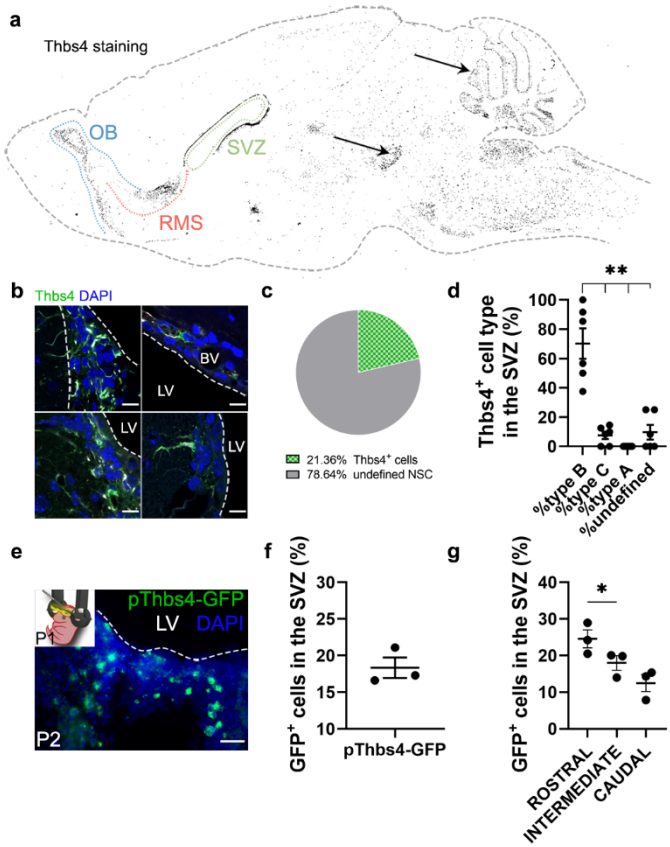

724

725 **Figure 1 – Thbs4 labels type-B cells in the SVZ neurogenic niche**. (a) Schematic drawing of the brain showing Thbs4
726 labeling throughout the mouse brain. Thbs4 was primarily found in the SVZ and RMS of the adult mouse telencephalon.
727 Arrows indicate non-specific Thbs4 staining in cerebellum and ventral tegmental area. (b) Thbs4 positive cells in the SVZ
728 displayed various morphologies. (c) Proportion of Thbs4-positive cells relative to the total NSCs population in the SVZ. (d)
729 Classification of Thbs4-positive cells in the SVZ based to their NSC morphology. (e) Electroporation of pThbs4-GFP at P1
730 revealed Thbs4 expression in the postnatal dorsal SVZ. (f) Quantification of Thbs4-reporter expression showing the proportion
731 of NSC expressing Thbs4 postnatally in the dorsal SVZ. (g) Thbs4-GFP reporter expression was upregulated in the rostral
732 SVZ. BV: Blood vessel; LV: Lateral ventricle. Scale bar = 10 µm (b) and 50 µm (e). Bars represent mean ± SEM. *$p < 0.05$
733 and **$p < 0.01$, Tukey post hoc test (after one-way ANOVA was significant at $p < 0.05$).

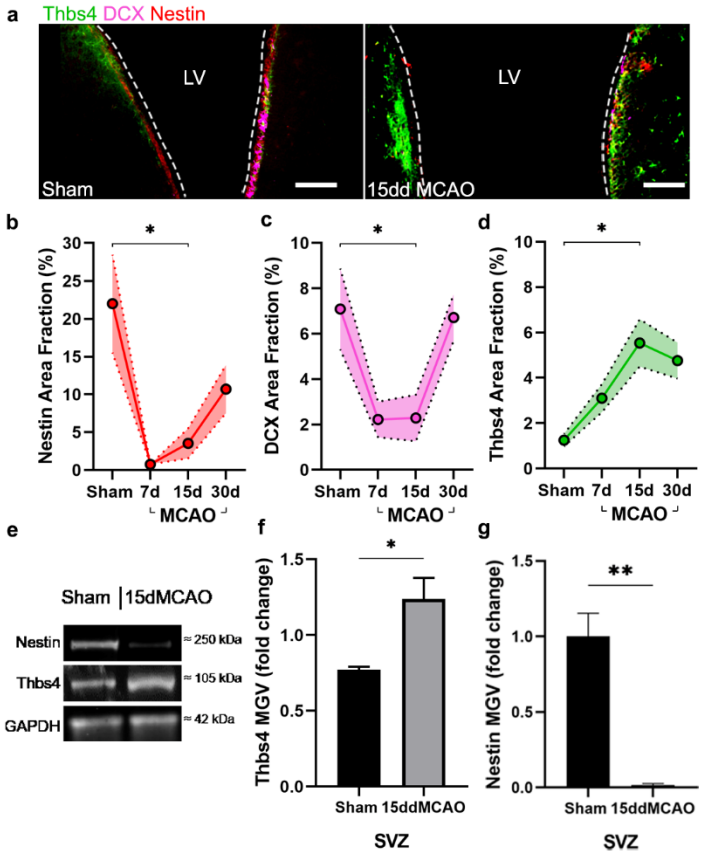

Figure 2 – Thbs4 expression is upregulated in the SVZ after brain ischemia. (a) Representative images of Thbs4 (green), Nestin (red) and DCX (magenta) in the SVZ under physiological conditions (left) and 15 days post-injury (dpi) (right). (b, c) The number of actively proliferating NSCs and neuroblast decreases at 7 and 15 dpi in the SVZ, as shown by reduced Nestin (b) and DCX (c) levels, respectively. (d) Thbs4 expression increases in the SVZ over time following ischemic injury. (e) Representative western blot images of Nestin and Thbs4 in sham and 15 dpi SVZ. (f, g) Quantification of mean gray value (MGV) from (e), normalized to GAPDH, shows an increased in Thbs4 (f) and a decrease in Nestin (g) in the 15 dpi SVZ. Scale bar = 100 µm in (a). n = 6 (b, c, d) and 3 (e, f, g) per condition. Bars represent mean ± SEM. *$p < 0.05$ and **$p < 0.01$; two-tail Student´s t test (sham vs. 15ddMCAO) and Tukey post-hoc test (after one-way ANOVA was significant at $p < 0.05$). See also Supplementary Figures 1 and 2.

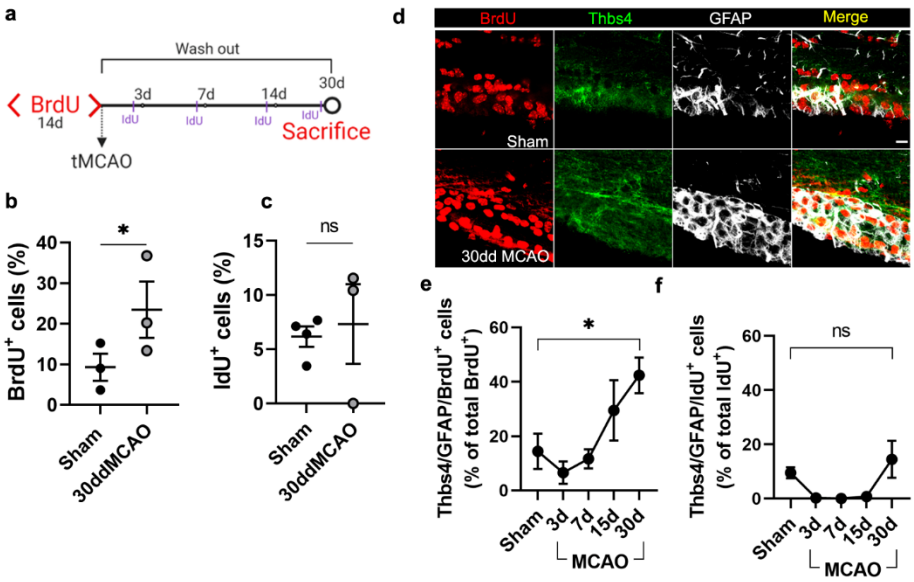

Figure 3 – Thbs4-positive cells derive from type-B NSCs in the SVZ after brain ischemia. (a) Experimental design: chronic BrdU (1% in water) treatment was administered for two weeks. BrdU labeling persisted only in B-type NSCs 30 days after treatment. Animals were injected with IdU (50 mg/kg) three times the day before euthanasia to label proliferating cells. (b, c) BrdU (b) and IdU (c) positive cells in the SVZ. Only BrdU-positive cells showed a significant increase at 30 dpi. (d) Representative confocal images showing Thbs4, GFAP and BrdU levels in sham (top) and 30 dpi mice (bottom). (e, f) Thbs4/GFAP/BrdU positive cells (slow proliferative cells) increased in the SVZ at 30 dpi (e), while no changes were observed in Thbs4/GFAP/IdU positive cells (fast proliferative cells). Scale bar = 10 µm (d). n = 4 (sham) and 3 (MCAO). Bars represent mean ± SEM. *$p < 0.05$ by two-tail Student´s t-test (sham vs. 30dd MCAO). See also Supplementary Figure 3.

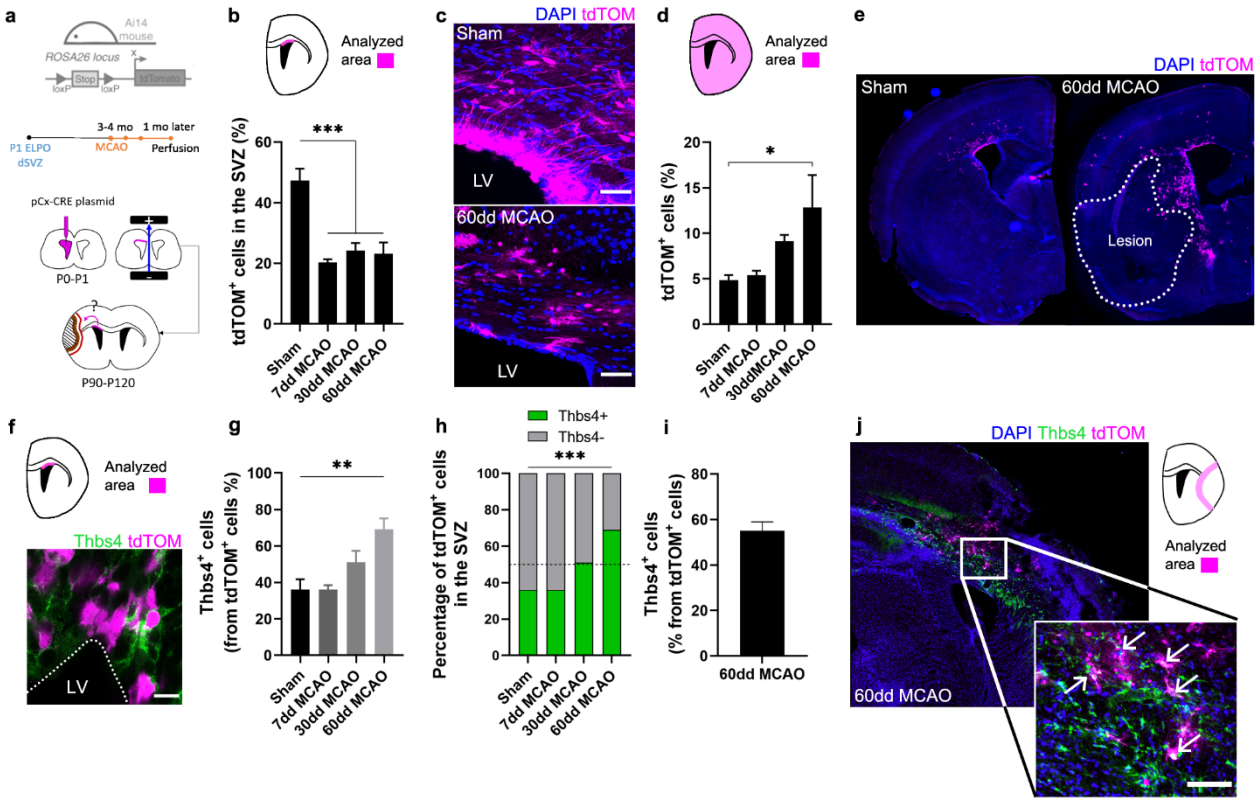

755

756 **Figure 4 – Ischemia-induced Thbs4 astrocytes migrate from the SVZ to ischemic areas.** (a) Experimental design: Ai14,
757 ROSA26-CAG-tdTomato transgenic mice were electroporated in the dorsal SVZ at P1. The pCAGGSx-CRE plasmid induced
758 tdTomato (tdTOM) expression in dorsal NSCs. MCAO was performed 3-4 months later in the same electroporated hemisphere.
759 Mice were analyzed at 7, 30, and 60 dpi. (b) Quantification of tdTOM-positive cells shows a decrease in the dorsal SVZ
760 following brain ischemia. (c) Representative images of tdTOM-positive cells in sham (top) and 60 dpi SVZ (bottom). (d)
761 Quantification of tdTOM-positive cells in the whole brain shows a gradual increase outside the SVZ after brain ischemia. (e)
762 Representative images of tdTOM expression in sham (left) and 60 dpi mice (right). (f) Representative image of Thbs4/tdTOM-
763 positive cells in the dorsal SVZ. (g) Quantification shows an increase in Thbs4/tdTOM-positive cells in the SVZ at 30 and 60
764 dpi. (h) The proportion of Thbs4-positive cells within the tdTOM-positive pool increases in the SVZ at 30 and 60 dpi. (i)
765 Around 50% of tdTOM-positive cells expressed Thbs4 in the infarcted tissue at 60 dpi. (j) Representative image of Thbs4 and
766 tdTOM expression near the damaged area. Scale bar = 50 µm (c), 10 µm (f), and 100 µm (g). n = 6 animals per condition. Bars
767 represent mean ± SEM. *$p < 0.05$, **$p < 0.01$, and ***$p < 0.001$ by Chi-square test (h) and Tukey post-hoc test (after one-
768 way ANOVA was significant at $p < 0.05$). See also Supplementary Figure 4.

769

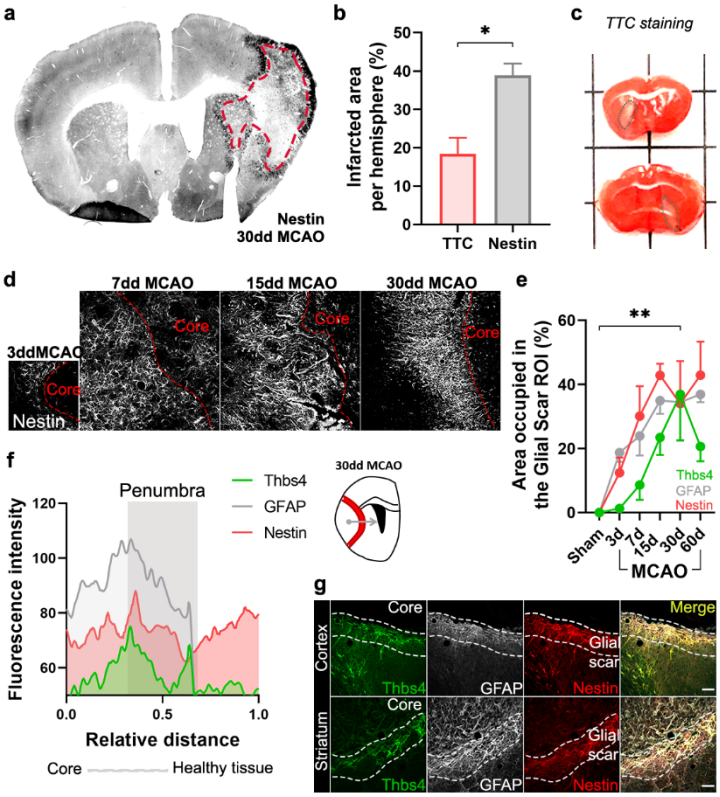

Figure 5 – Ischemia-induced Thbs4 astrocytes accumulate at the glial scar. (a) The glial scar could be observed at 30 dpi using Nestin immunofluorescence. (b) Classical TTC technique underestimated ischemic regions compared with Nestin immunofluorescence. (c) Representative images of TTC staining in infarcted brains. (d) Representative confocal images showing the time course of Nestin expression at 3, 7, 15 and 30 dpi. (e) The Nestin-positive glial scar was established by 15 dpi, while Thbs4 astrocytes arrived at the glial scar later, by 30 dpi. (f) Fluorescence profile of Thbs4, GFAP and Nestin marker from the core to penumbra areas shown Thbs4 was mainly located at the borders of the Nestin-positive glial scar. (g) Representative images of Thbs4 (green), GFAP (white) and Nestin (red) markers in sham (top) and 30 dpi mice (bottom). Scale bar = 50 µm (g). n = 3 animals per condition. Bars/lines represent mean ± SEM. *$p < 0.05$ and **$p < 0.01$ by two-tail Student´s t test (TTC vs. Nestin) and by Dunnett posthoc test (after two-way ANOVA was significant at $p < 0.05$). See also Supplementary Figure 5.

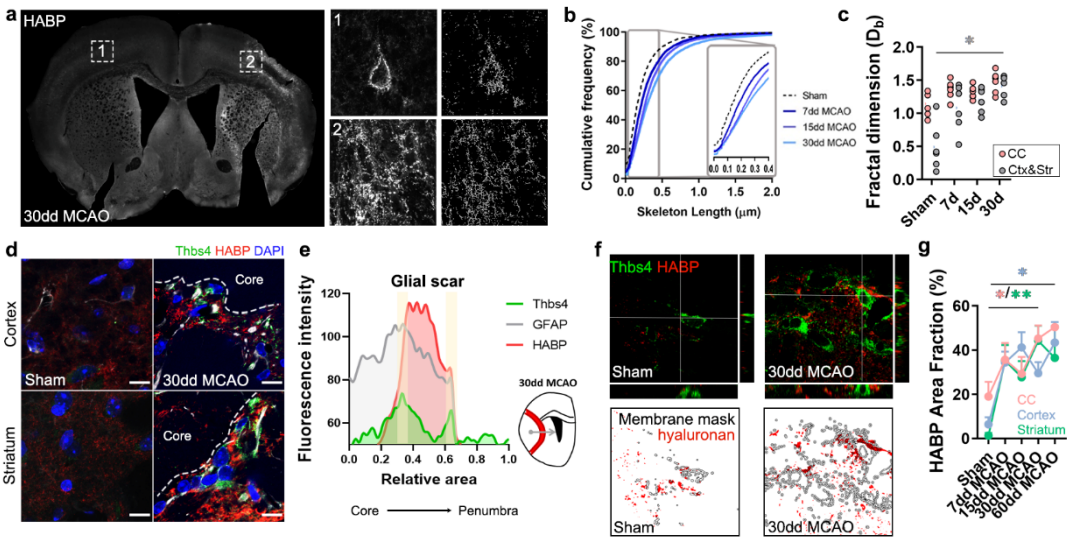

Figure 6 – Thbs4-positive astrocytes produce hyaluronan at the glial scar after MCAO. (a) Representative images of hyaluronic acid (HA) labeled with HABP in the contralateral (1) and ipsilateral hemisphere (2). Only perineuronal nets are clearly visible in the healthy tissue, while a dense interstitial matrix is observed in ischemic areas. (b) Cumulative distribution of skeletonized HA signal in sham and infarcted regions of 7, 15 and 30 dpi mice ($p < 0.0001$). (c) Quantification of fractal dimension showed increased extracellular matrix interconnectivity in the infarcted cortex and striatum (Ctx & Str) at 30 dpi. (d) Representative confocal images of Thbs4 (green) and HABP (red) in the cortex and striatum of sham and 30 dpi mice. Note the HA labelling on the surface of Thbs4-positive cells. (e) Fluorescence intensity profile of Thbs4, GFAP and HABP markers from the lesion core to penumbra areas. Thbs4 expression was mainly restricted to the borders of the HA-positive glial scar at 30 dpi. (f) Representative confocal images of Thbs4 and HABP markers in sham and 30 dpi mice (top). Examples of HA (red) occupying the membrane mask of Thbs4-positive astrocytes in sham and 30 dpi mice (bottom), showing increased HA synthesis after MCAO. (g) Quantification of membrane-bound HA showed increased HA along Thbs4-positive membrane after brain ischemia (corpus callosum: pink; infarcted cortex: blue; infarcted striatum: green). Scale bar = 10 µm (e). n = 6 animals per condition. *$p < 0.05$ and ****$p < 0.0001$ by Krustal Wallis test and two-way ANOVA (significant at $p < 0.05$). See also Supplementary Figures 6 and 7.

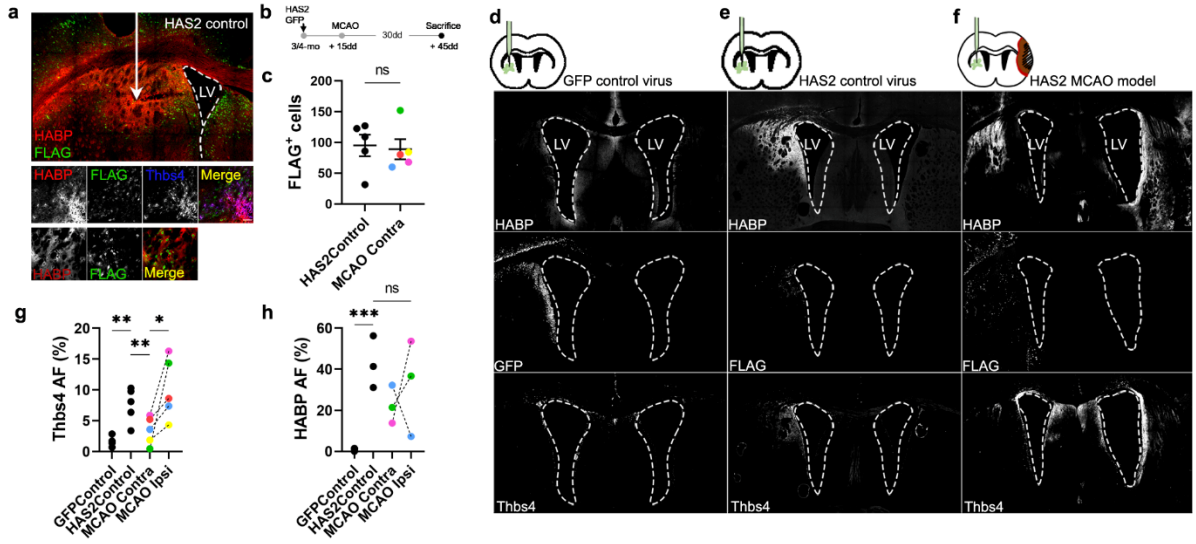

Figure 7 – Hyaluronan accumulation is sufficient but not exclusive to recruit Thbs4 astrocytes. (a) Representative images of HA accumulation caused by viral-mediated overexpression of HAS2 from naked mole rat. (b) Experimental design: HAS2 viral injections were performed 2 weeks before MCAO. Animals were sacrificed 30 days after MCAO. We used standard GFP virus as control. Two groups of HAS2-injected mice were studied, with only one subjected to MCAO. (c) FLAG-positive cells (HAS2 virus tag) did not show changes in either HAS2 control (HAS2Control) or HAS2-MCAO group (contralateral hemisphere). (d, e, f) Representative images of HABP, GFP and Thbs4 markers in GFP control virus (d), HAS2 control virus (e) and HAS2 MCAO group (f). (g) Thbs4 expression increased after HAS2 viral-mediated overexpression. However, Thbs4 was upregulated in the ischemic hemisphere when MCAO was performed together with the HAS2 viral infection (MCAO ipsi). GFP control virus did not induce increase of Thbs4. (h) HABP was used as a control for HA accumulation. Thbs4 astrocytes in HAS2 MCAO group increased in the ischemic hemisphere even though HA accumulation in both hemispheres (HAS2 and MCAO hemisphere), suggesting additional ischemia-induced signals recruit Thbs4 astrocytes to infarcted areas. Scale bar = 100 µm (a). n = 6 animals per condition. *$p < 0.05$, **$p < 0.01$ and ***$p < 0.001$ by two-tail Student´s t-test (HAS2Control vs. MCAO Contra) and Tukey posthoc test (after one-way ANOVA was significant at $p < 0.05$).

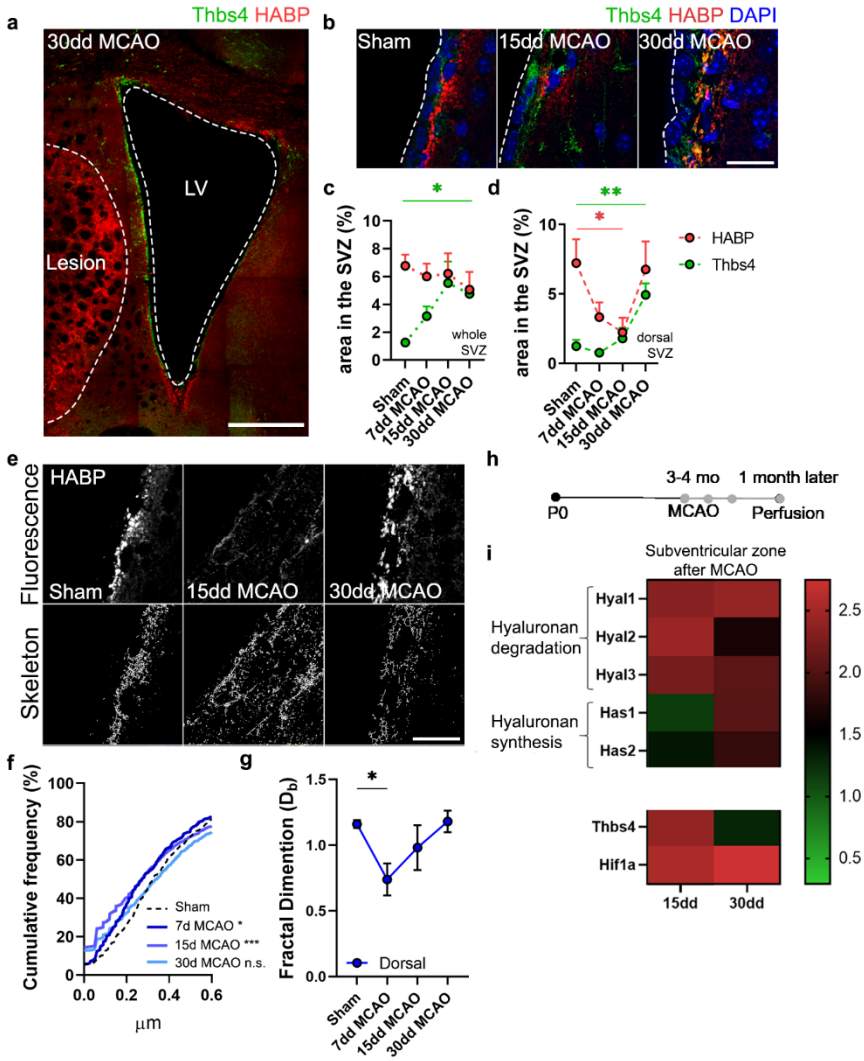

Figure 8 – HA degradation in the SVZ correlates with Thbs4 response to brain ischemia. (a) Representative image of Thbs4 and HA (HABP) markers in the SVZ at 30 dpi. (b) Representative images of Thbs4 and HA in the sham and 15, 30 dpi SVZ. (c, d) HA levels did not change in the entire SVZ after MCAO (c) but decreased significantly in the dorsal SVZ (d). Thbs4 expression increased throughout the SVZ after MCAO (c), with a marked rise at 30 dpi in the dorsal SVZ (d), coinciding with HABP reduction. (e) Representative confocal (top) and skeletonized (bottom) images of HABP in the dorsal SVZ of sham, 15 and 30 dpi mice. (f) Cumulative distribution of HA skeletons showed a reduction in the length of HA cable-like structures only in the dorsal SVZ at 7 and 15 dpi. (g) The interconnectivity of the extracellular matrix decreased by 7 dpi in the dorsal SVZ, as measured by fractal dimension. (h) Experimental design for qPCR: 3–4-month-old mice were subjected to MCAO, and fresh SVZ tissue was extracted 15 and 30 days after MCAO for RT-qPCR analysis. (i) Hyaluronan degradation genes (Hyal1, Hyal2 and Hyal3) increased by 15 and 30 dpi in the SVZ, while hyaluronan synthase genes (HAS1 and HAS2) were overexpressed later, at 30 dpi. Thbs4 and Hif1a were also upregulated by 15 and 30 dpi in the SVZ. Scale bar = 100 µm (a). n = 6 (c, d, e and g) and 3 (i). *$p < 0.05$, **$p < 0.01$ and ***$p < 0.001$ by Krustal Wallis test and Tukey post-hoc test (after one-way ANOVA was significant at $p < 0.05$).

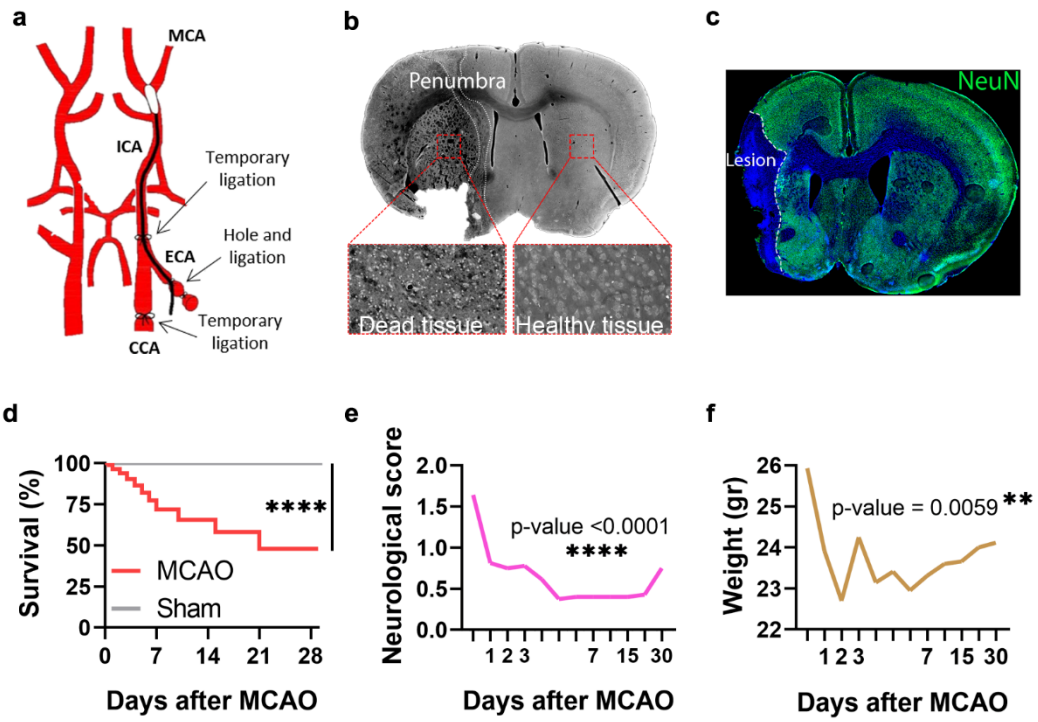

Supplementary Figure 1 – Characterization of the Middle Cerebral Artery Occlusion (MCAO) mouse model of brain ischemia. Related to Figure 2. (a) Scheme of the procedure: 10 mm silicon-coated filament was inserted through an external artery and re-directed to the internal one. Ischemia was induced after 60 minutes of occlusion. After that, the filament was removed, and animals were observed every day before euthanasia. (b) Volume of infarction was observed by cresyl violet staining. (c) Neuronal death was observed by NeuN immunofluorescence. (d) Around 50% of ischemic mice survived at 28 dpi. (e) Ischemic animals ameliorated neurological symptoms over time. (f) Weight was measured as controls for mice healthcare. n = 17 (d, e, f). $^{**}p < 0.01$ and $^{****}p < <0.0001$ by survival curve test and Tukey post-hoc test (after one-way ANOVA was significant at $p < 0.05$).

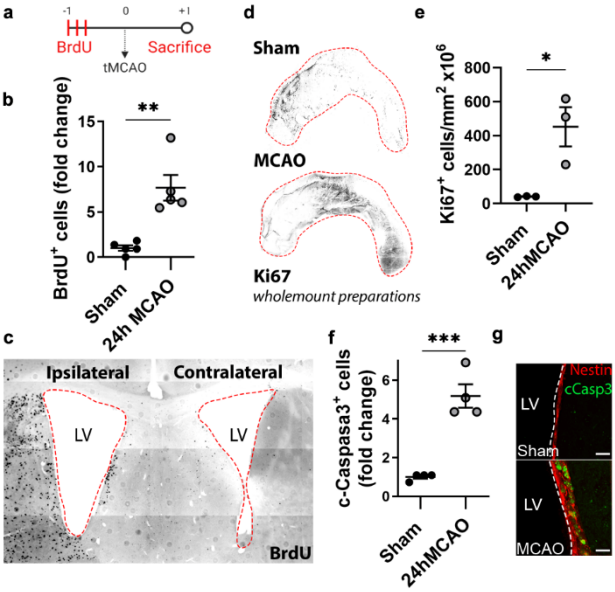

Supplementary Figure 2 – Cell proliferation in the SVZ after brain ischemia. Related to Figure 2. (a) Experimental design: three BrdU (50mg/kg) injections were performed the day before MCAO protocol. Animals were sacrificed 24 hours after the brain stroke model. (b) BrdU-positive cells increased in the SVZ 24 hours after MCAO. (c) Representative image of BrdU positive cells in the ipsilateral (left) and contralateral (right) hemisphere 24 hours after MCAO. (d) Ki67 marker was also used to analyze cell proliferation in wholemount preparations of the SVZ. (e) Ki67 positive cells increased in the SVZ 24 hours after MCAO. (f) The Cleaved-Caspase 3 marker increased in the SVZ 24 hours after MCAO. (g) Cleaved-caspase 3 marker was used to assess apoptosis in the SVZ after brain ischemia. Scale bar = 15 µm (g). n = 5 (sham) and 4 (MCAO). Bars represent mean ± SEM. *$p < 0.05$, **$p < 0.01$ and ***$p < 0.001$ by two-tail Student´s t-test (sham vs. 24h MCAO).

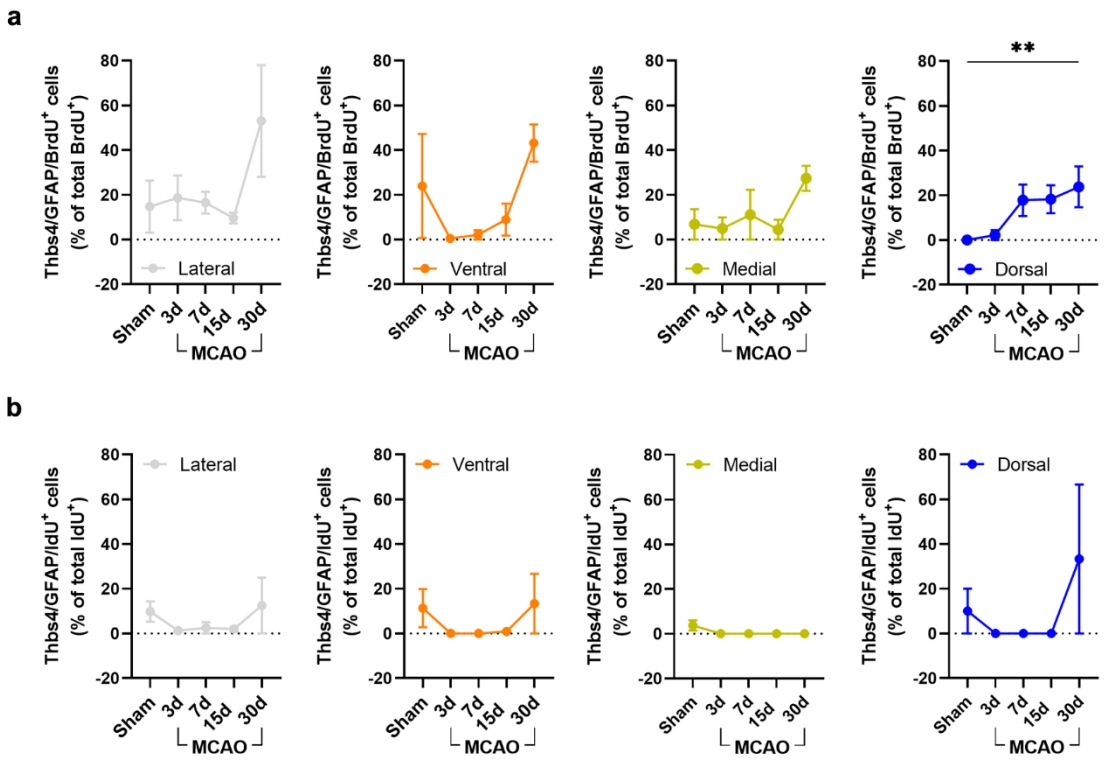

848

849 **Supplementary Figure 3 – Thbs4 astrocytes derive from slow proliferative cells after brain ischemia.** Related to Figure
850 3. (a) Slow proliferative cells were quantified in the lateral (grey), ventral (orange), medial (yellow) and dorsal (blue) SVZ.
851 We only observed an increase of Thbs4/GFAP/BrdU positive cells in the dorsal SVZ 30 dpi. (b) Thbs4/GFAP/IdU positive
852 cells did not show changes in the lateral (grey), ventral (orange), medial (yellow) and dorsal (blue) SVZ after brain ischemia.
853 n = 4 (sham) and 3 (MCAO). $^{**}p < 0.01$ by by two-tail Student´s t-test (sham vs. 30dd MCAO).

854

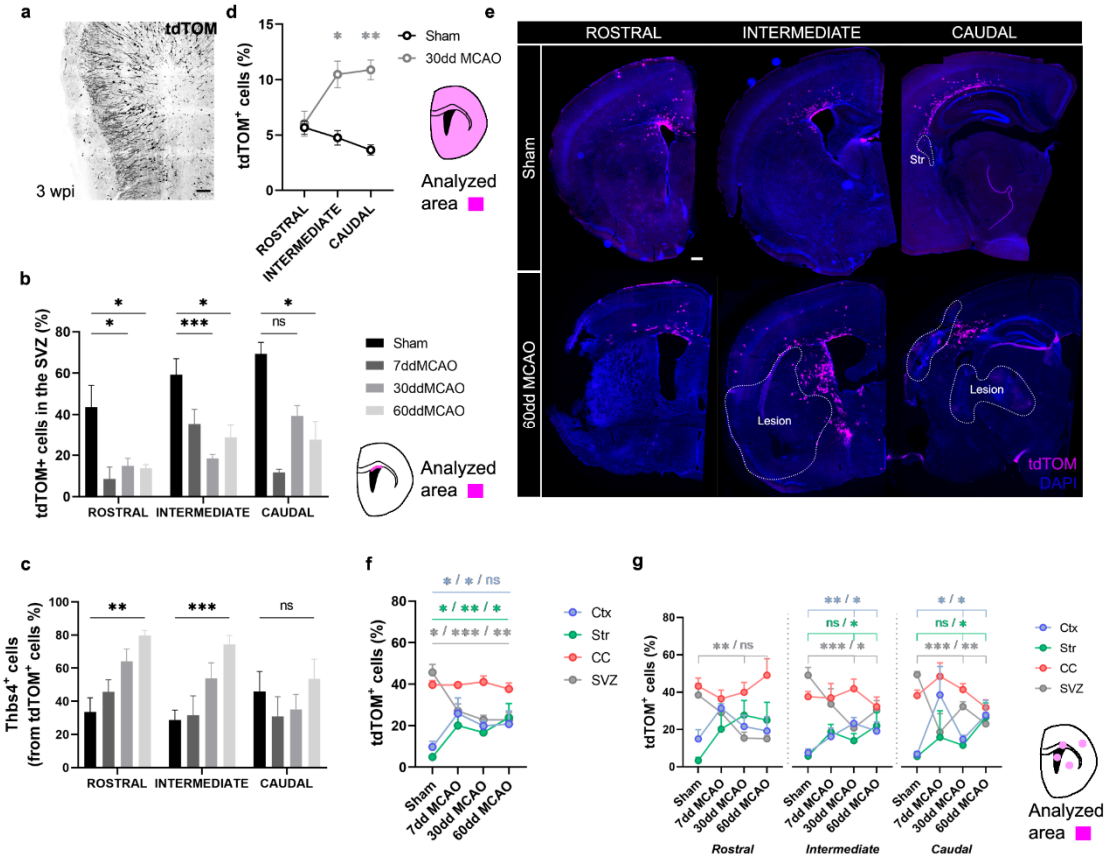

Supplementary Figure 4 – Ischemic-induced Thbs4 astrocytes migrate preferentially to caudal infarcted areas. Related to Figure 4. (a) Representative image of tdTOM positive cells in the OB three weeks after electroporation (3wpi). (b) tdTOM-positive cells decreased in the rostral, intermediate and caudal SVZ 7, 30 and 60 dpi. (c) Thbs4/tdTOM positive cells increased in rostral and intermediate SVZ 30 and 60 dpi. (d) Expression of tdTomato increased in intermediate and caudal brain areas at 30 dpi. (e) Representative images of tdTOM expression in rostral (left), intermediate (middle) and caudal (right) brain areas of sham (top) and 60 dpi mice (bottom). (f) tdTOM positive cells increased in the infarcted cortex (Ctx) and striatum (Str) whereas decreased in the dorsal SVZ (SVZ). No changes were observed in the corpus callosum (CC). (g) tdTOM positive cells only increased in the infarcted cortex and striatum at intermediate and caudal brain regions. Scale bar = 100 µm (a) and 1000 µm (e). n = 6 animals per condition. Bars represent mean ± SEM. *$p < 0.05$, **$p < 0.01$ and ***$p < 0.001$ by Dunnett/Tukey post-hoc test (after two-way ANOVA was significant at $p < 0.05$).

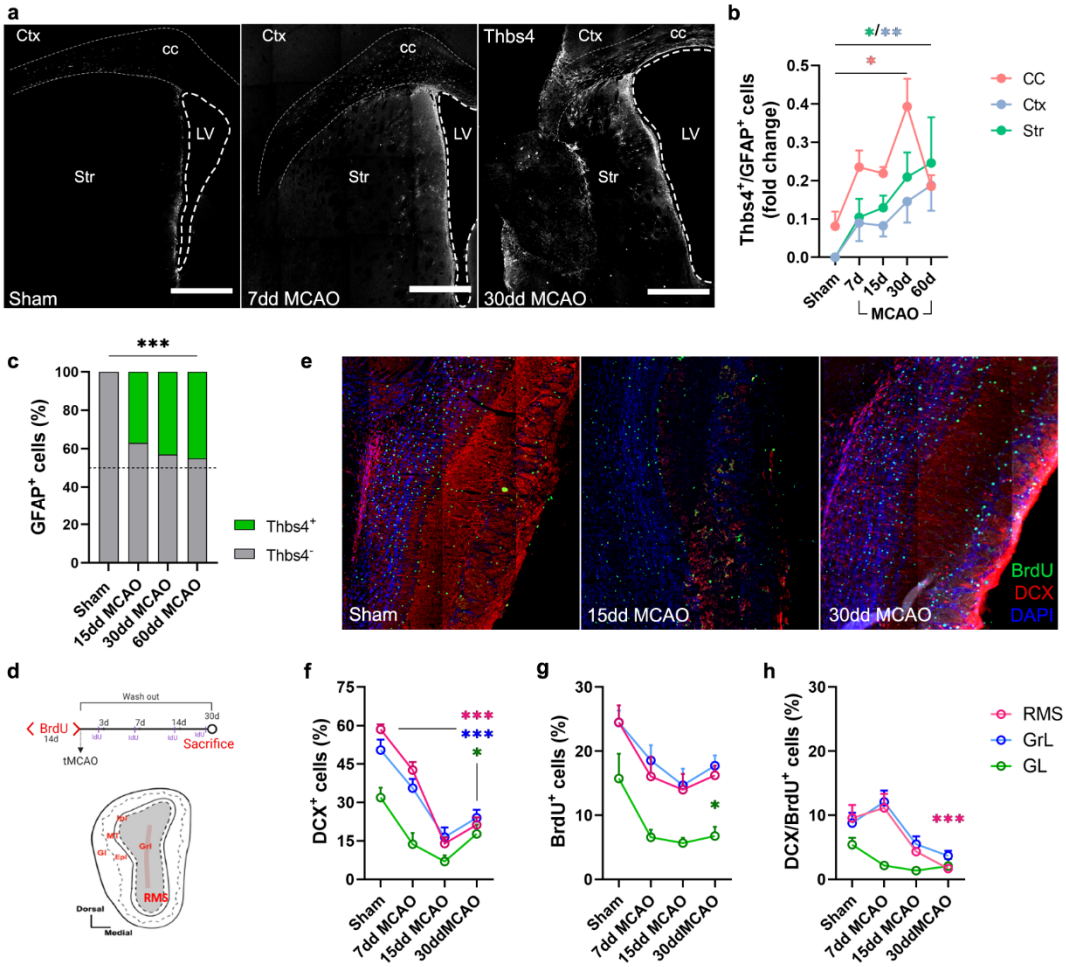

866 **Supplementary Figure 5 – SVZ NSC stop producing newborn neurons to send newborn astrocytes to the ischemic**
867 **areas.** Related to Figure 5. (a) Thbs4 expression in the corpus callosum (cc), infarcted cortex (Ctx) and infarcted striatum
868 (Str) of sham and 7 and 30 dpi mice. (b) Thbs4 increased by 30 dpi in the corpus callosum (cc) and 60 dpi in the infarcted
869 cortex (Ctx) and infarcted striatum (Str). (c) Expression of Thbs4 increased in total GFAP population after 15, 30 and 60 dpi.
870 (d) Experimental design: chronic BrdU (1% in water) treatment was administered for two weeks. BrdU only persisted in
871 slow proliferative NSC (Codega et al., 2014). DCX and BrdU positive cells were measured in the OB layers 7, 15 and 30
872 dpi. (e) Representative images of BrdU and DCX marker in sham (left), 15 (middle) and 30 (right) dpi mice OB. (f) DCX
873 positive cells decreased 15 and 30 dpi in the RMS, granular OB layer (GrL) and glomerular OB layer (GL). (g) BrdU
874 positive cells only decreased 30 dpi in the glomerular OB layer (GL). Double DCX/BrdU positive cells significative
875 decreased in the RMS 30 dpi. In (f) and (g), values are normalized to total DAPI nuclei (100%). Scale bar = 500 µm (a). n =
876 6 animals per condition. Lines represent mean ± SEM. *$p < 0.05$, **$p < 0.01$ and ***$p < 0.001$ by Chi-square test and Tukey
877 post-hoc test (after two-way ANOVA was significant at $p < 0.05$).

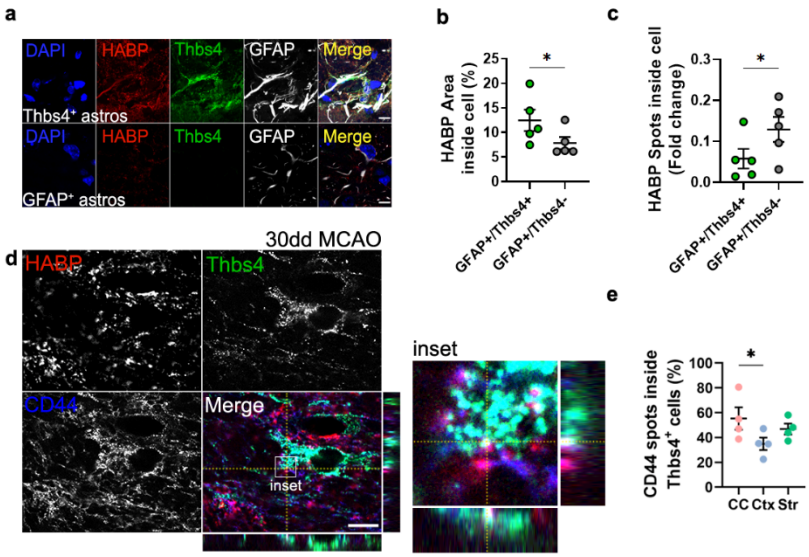

Supplementary Figure 6 – Thbs4 astrocytes internalize HA in the infarcted areas. Related to Figure 6. (a) Representative images of Thbs4/GFAP ("newborn astrocytes", top) and GFAP-only ("local astrocytes", bottom) cells in the infarcted areas at 30 dpi. (b) Thbs4-positive astrocytes internalized more HA compared to local astrocytes only labelled with GFAP marker. (c) However, the number of HA spots internalized was higher in local astrocytes compared with Thbs4 astrocytes, suggesting that Thbs4 internalize HA in fewer vesicles. (d) Representative images of HABP (red), Thbs4 (green) and CD44 (blue) at the lesion border. Inset shows an orthogonal projection of Thbs4/CD44/HABP-positive intracellular vesicle. (e) Thbs4 positive astrocytes expressed a high rate of CD44 receptors so much in corpus callosum (CC), infarcted cortex (Ctx) as in infarcted striatum (Str). Scale bar = 10 µm (c, f). n = 5 animals per condition. Bars represent mean ± SEM. *$p < 0.05$ and **$p < 0.01$ by Tukey posthoc test (after two-way ANOVA was significant at $p < 0.05$) and two-tail Student´s t-test (Thbs4 vs GFAP).

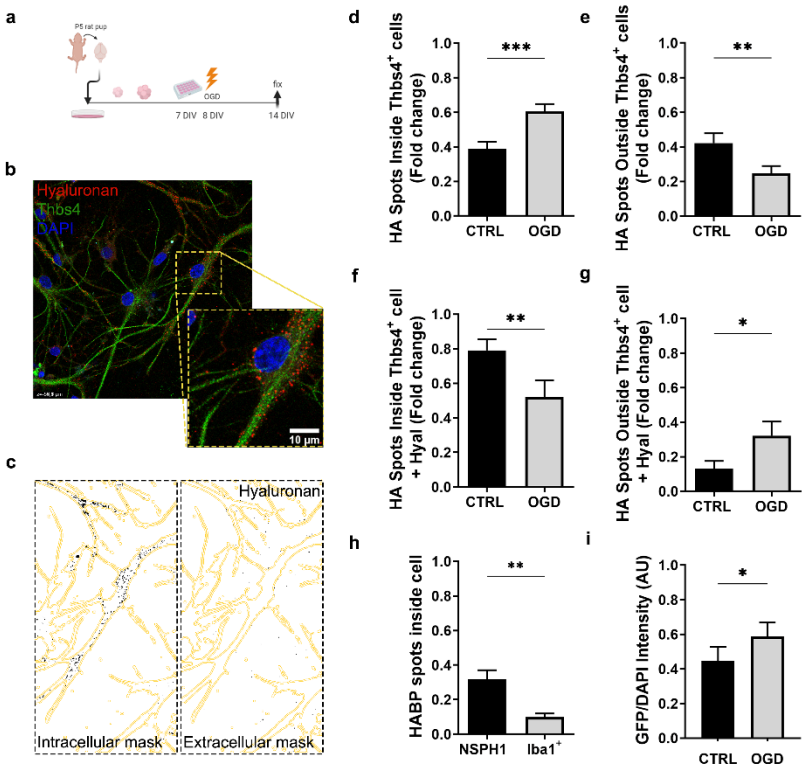

Supplementary Figure 7 – In vitro NSC-derived Thbs4 cells synthetize HA after a hypoxic-ischemic condition. Related to Figure 6. (a) Experimental design: P4 pup rats were sacrificed, and SVZ NSC were extracted and cultured in the proliferative medium for one week. After that, neurospheres were disaggregated and seeded isolated in a culture dish. The following day, oxygen and glucose deprivation protocol (OGD) was performed. Cells were fixed 7 days after culture them. (b) Representative images of in vitro Thbs4 positive cells (green) and HA (red). (c) HA spots were measured inside and outside Thbs4 positive cells. (d) HA spots increased inside Thbs4 positive astrocytes after OGD whereas (e) decreased in the extracellular space. However, when NSC were exposed to hyaluronidases in order to remove extracellular HA, Thbs4 positive cells decreased internalization of HA spots (f) and increased extracellular HA spots (g). (h) Neurosphere-derived NSC (NSPH1) internalized more HA spots compared with Iba1-positive cells. (i) Metalloproteinase activity was higher in OGD NSC cultures compared to control condition. Scale bar = 10 µm (b). n = 15 samples per condition. Bars represent mean ± SEM. *$p < 0.05$, **$p < 0.01$ and ***$p < 0.001$ by two-tail Student´s t-test (CTRL vs. OGD; NSPH1 vs. Iba1^{+}).

902

Table 1. Primary antibodies used for in vivo immunofluorescence protocol

Antibody	Host	Isotope	Dilution	Reference	Company
Thbs4	Mouse	Monoclonal IgM kappa light chain	1/400	Sc-390734	Santa Cruz Biotechnology, USA.
Thbs4	Goat	Polyclonal IgG	1/200	AF2390	R&B systems, USA
S100β	Rabbit	Polyclonal	1/400	Z0311	Dako, Agilent Technologies, Inc.
S100β	Mouse	Monoclonal IgG2a	1/1000	MA5-12969	Invitrogen, Spain
GFAP	Mouse	Monoclonal IgG1	1/1000	MAB3402	Sigma, Spain
GFAP	Rabbit	Polyclonal	1/4000	Z0334	Dako, Agilent Technologies, Inc.
βIII tubulin	Rabbit	Polyclonal	1/400	ab18207	Abcam, UK
NeuN	Mouse	Monoclonal IgG1	1/1000	MAB377	Millipore, Germany
DCX	Rabbit	Polyclonal IgG	1/500	ab18723	Abcam, UK
Nestin	Chicken	Polyclonal IgY	1/1000	NES	Aves Lab, EEUU
Prominin 1	Rat	Monoclonal IgG1 kappa	1/300	14-1331-82	Invitrogen, Spain
EGFR	Mouse	Monoclonal	1/400	SAB4200809	Abcam, UK
BrdU	Rat	Monoclonal	1/400	MCA2060	Bio-Rad, USA.
BrdU	Mouse	Monoclonal IgG1, kappa	1/500	03-3900	Invitrogen, Spain
IdU	Mouse	Monoclonal IgG2b	1/100	MA5-24879	Invitrogen, Spain
Ki67	Rabbit	Polyclonal IgG	1/400	Ab15580	Abcam, UK
Cleaved-Caspase 3	Rabbit	Monoclonal IgG	1/300	#9664	Cell Signaling, Germany
CD44	Rat	Monoclonal IgG2b	1/500	MA517875	Invitrogen, Spain
FLAG	Mouse	Monoclonal IgG1	1/500	F1804	Sigma, Spain
Olig2	Mouse	Monoclonal IgG2aκ	1/1000	MABN50	Millipore, Germany

903

Table 2. Primer sequences for qPCR

904

Name	Sequence
Hyal1_FW	GTGCCAAGCCCTATGCTAATAAG
Hyal1_REV	GCATGTCCATTGCAAAGACTGA
Hyal2_FW	GTCCCACATACACCCGAGGA
Hyal2_REV	GGCACTCTCACCGATGGTAGA
Hyal3_Ffw	GGACGACCTGATGCAGACTATTG
Hyal3_REV	GGTCCCCCCAGAGTACCACT
Has1_FW	AGGGCTCTTAAAGGAGGAGTCC
Has1_REV	AGAAGGTAAACTGAGTCCCCAGAA
Has2_FW	CAAAGAGGTTCGTTCAAGTTCTGA
Has2_REV	TGTGTTTGTTTCCCACTAGCTCTC
Hif1a_FW	CATAAAGTCTGCAACATGGAAGGT
Hif1a_REV	ATTTGATGGGTGAGGAATGGGTT
HPRT1_FW	TGATAGATCCATTCCTATGACTGTAGA
HPRT1_REV	AAGACATTCTTTCCAGTTAAAGTTGAG

905